Multifunctional Transceiver for Future Radar Sensing and Radio Communicating Data-Fusion Platform

JABER MOGHADDASI, (Student Member, IEEE), AND KE WU, (Fellow, IEEE)

Poly-Grames Research Center, Centre de Recherche en Électronique Radiofréquence, Department of Electrical Engineering,
École Polytechnique de Montréal, University of Montreal, Montreal, QC H3T 1J4, Canada

Corresponding author: J. Moghaddasi (jaber.moghaddasi@polymtl.ca)

ABSTRACT A unified and reconfigurable multifunctional transceiver for future integrated data-fusion services of radar sensing and radio communication (RadCom) is studied and developed in this paper. This proposed alternative of the state-of-the-art architectures presents an unprecedented integration of all radar sensing and RadCom functions together in a time-division platform. Furthermore, it is capable of offering a positioning function of both moving and static objects with an enhanced resolution in ranging in addition to providing a greater capability of data communication. The design and the performance incompatibilities between radar and radio systems are explored and investigated. A systematic top–bottom approach is presented, which involves the step-by-step methodology, building block design considerations, and the system level simulation. With the purpose of validating the proposed scheme, a low-frequency prototype around the FCC-commissioned dedicated short range communication (DSRC) band is developed, and its performance is evaluated. Since such a unified transceiver can find applications in intelligent transportation infrastructures, the system demonstrator is designed and examined according to the desired specifications of future automotive radar networks. Through various system level measurements, the proposed scheme has demonstrated attractive features in connection with both radar and radio functions. With the radar mode, the added ability of angle detection and the improved range resolution against the previously demonstrated version make the system suitable for driving assistance applications. With the radio mode, the system demonstrator has proved a great capability of communication at a data rate of 25 Mb/s.

INDEX TERMS Intelligent transportation system (ITS), multifunctional transceiver, software-defined system, positioning technique, radar sensing, radio communication, RF vehicular technology.

I. INTRODUCTION

In the 1990s, the concept and technology of intelligent transportation system (ITS) was introduced and studied for the first time [1]. ITS encompasses a broad range of technologies, supporting two indispensable functionalities, namely environmental sensing and sensory-data communicating services including vehicle-to-vehicle (V2V) communications. The ITS development has not achieved all its predefined objectives and potentials even though this concept is now more than twenty years old. That is because a successful marketing of ITS demands for low cost, highly efficient, and small form factor vehicular products while realizing a variety of required functions also demands for utilizing different expensive sensor and radio systems. Assembling different system modules on a single platform should not be the optimum solution. Therefore, significant research activities for developing sensor fusion techniques [2] and integrated

radar and communication (radio) devices through transceiver unification [3] have come into play. The concept of radar-communication unification originates mainly from [4], which is further developed and termed as ''RadCom'' in this work for simplicity.

Interestingly, the search for the most efficient solution in connection with multifunctional systems has progressed in a few different directions. The differentiating aspect of all reported outcomes is related to the integration scheme that involves waveform and the associated transceiver architectures. Furthermore, such a functional integration may take part in frequency domain through either multicarrier or spread spectrum techniques [5]–[13], or in time domain through time-division technique [14]–[16].

Either time or frequency domain based integration scheme possess specific advantages or disadvantages that may make them preferable depending on the desired functionality and

tolerable cost or complexity of the system. The nature of the already reported schemes along with their pros and cons can be found in [15].

The main advantage of time division over frequency division is the efficient usage of frequency resources, especially around narrow available frequency bands. With the former approach, the whole band might be allocated to radar sensing in support of a good resolution during the radar cycle while the same band can be divided into several narrower segments to be used for communication between units in different cells. However, the major drawback of time-domain integration scheme is the necessity of synchronization. Indeed, units in the same system cell should use the same carrier frequency, and the reference clock signal of all units in a system cell should be synchronized. This can be done, using the timing information of global positioning system (GPS) or even other techniques such as network time protocol [17].

Apart from the integration domain, in all RadCom systems, the well-known techniques of wireless sensing and communications are incorporated. The main challenge remains for the development of transceiver architectures in which techniques for RF component unification or sharing should be applied in order to avoid high cost and complexity. This issue becomes rather important when more functions are desired to be added to these multi-functional systems.

The radar associated functions in the majority of reported RadCom schemes are limited to merely range and velocity estimation, and rarely a solution is presented for complete object positioning via an additional function of angle detection, while this is an indispensable function of automotive radar systems. Furthermore, the technique of time-difference-of-arrival (TDOA) is adopted in RadCom system proposed by [18] which uses pulse-position-modulation (PPM) as operational signal and is capable of complete localization, and also the concept of incorporating OFDM RadCom systems with multiple-input-multiple-output (MIMO) architectures is discussed through simulations in [19].

Existing techniques of angle detection demand for utilizing at least two receiver channels. Hence, incorporating them in RadCom systems may undesirably augment the complexity in implementation unless every portion of the transceiver is unified or shared if separation is not inevitable.

In this work, our focus is on the development of in-time-domain integrated RadCom systems with an intended application around dedicated short range communication (DSRC) band where a very narrow bandwidth is available. The function of angle detection is added by employing the Doppler and beat signal's phase-difference of arrival. Therefore, a new transceiver architecture is proposed. To address the simplicity and compactness, some essential portions in the Tx block are implemented in a software manner and a switching technique is applied to share the components in Rx block.

Additionally, the features of the in-time-domain integrated RadCom waveform is studied further in detail and the techniques that can be applied to meet the intended specifications of the proposed RadCom transceiver are re-examined concisely. The severe incompatibility of radar and radio channels and systems are also analyzed and accordingly a new transceiver architecture is proposed and prototyped. The functionality of the whole transceiver is validated through both system-level simulations and measurements. Early results of this effort have been presented by authors in [20] and a comprehensive discussion is presented in this paper along with extensive measurement results and details. In the end, the limitations of current systems along with the capabilities of further research and developments of RadCom systems are concluded.

II. SYSTEM CONCEPT
A. SIGNAL MODULATION SCHEME
Fig. 1 shows the spectrogram of power spectral density (PSD) of an operational signal of our time-domain RadCom system that was probed using a digital oscilloscope (Agilent-DSO81204B) and analyzed by a commercial software of vector signal analyzer (Agilent-VSA89600). The signal is generated by a combination of field programmable gate array (FPGA) and direct digital synthesizer (DDS).

The frequency-versus-time diagram of the signal in Fig. 1(a) shows that it consists of a trapezoidal FMCW (TFMCW) that is followed by a single frequency carrier in the middle of the band. The TFMCW may appear occasionally as radar cycle for sensing the environment while the single frequency carrier pertains to communication cycle and can be phase-modulated by information data as it is shown in Fig. 1(b). This waveform can be considered as a function of time within the following expression.

$$S^{Tx}(t) = \mathrm{Re} \times \left\{ \begin{array}{ll} Ae^{j2\pi(0.5\Gamma t^2 + f_1 t)} & 0 \leq t \leq T_c \\ Ae^{j2\pi(f_2(t-T_c))} & T_c \leq t \leq 2T_c \\ Ae^{j2\pi(-0.5\Gamma(t-2T_c)^2 + f_2(t-2T_c))} & 2T_c \leq t \leq 3T_c \\ \sqrt{I^2+Q^2}e^{j2\pi\left(f_c(t-3T_c)+\tan^{-1}\left(\frac{Q(t)}{I(t)}\right)\right)} & 3T_c \leq t \leq 4T_c \end{array} \right\}$$

$$(1)$$

where Γ is the chirp's slope, T_c is the time slot duration, and f_1 and f_2 are lower and upper sides of chirps, respectively. It should be noted that the carrier position for communication may vary along the frequency axis and thereby onboard units may use a frequency division multiple access (FDMA) technique and hence increase the network capacity.

B. OPERATION PRINCIPLES
With this time-agile waveform scheme and the use of a software-defined signal source, the system is able to operate as either radar or radio in a reconfigurable manner. A typical scenario is shown in Fig. 2. All on onboard units must be synchronized and operate within the identical mode, i.e., radar or radio ones.

As a radio for communication, onboard units must work through time division duplexing (TDD) and it may not transmit and receive data, simultaneously. Hence, any single unit
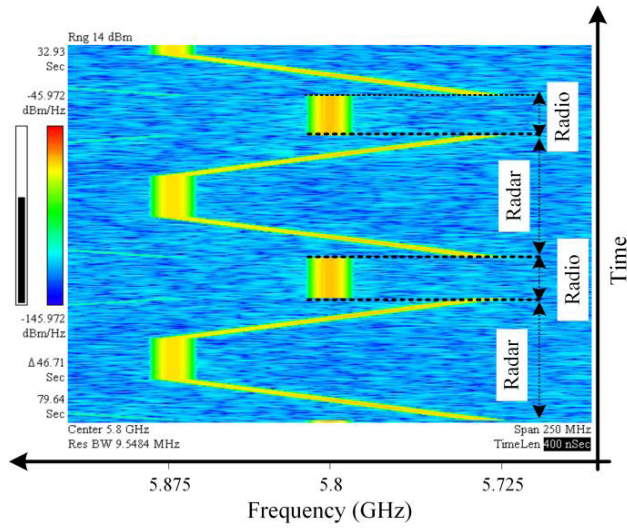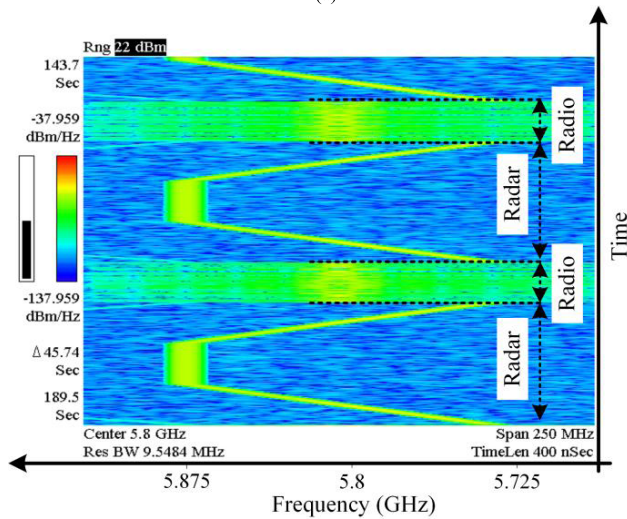
FIGURE 1. Spectrogram of power spectral density (PSD) of the operational signal for the proposed RadCom system for two modes of operation. The signal is generated by a combination of FPGA and DDS boards, and is probed by a digital oscilloscope. Frequency and phase of the signal vary so that the system can realize required functions of sensing and communicating. (a) Single carrier for communication is not modulated. (b) Single carrier for communication is modulated in phase.

FIGURE 2. Typical application scenario; In radar time cycle all on-board units are sensing the environment while they can communicate and exchange the sensory data in radio time cycle. A radar network can be made through data fusion which can increase the range of coverage. (a) Radar mode. (b) Communication mode.

may not receive data from other units while it is sending information data to others. Indeed, in order to communicate as a receiver, the unit must sustain the carrier intact and use it as LO for the quadrature demodulator in receiver. Let's take an example of the two onboard units which intend to communicate. If unit 1 wants to transmit data, it should modulate its carrier while unit 2 keeps the carrier un-modulated and uses it for quadrature demodulation of the received signal from unit 1. The minimum communication time slot duration should be equal to the Tx/Rx switching interval in the adopted TDD scheme. In multiuser environments, TDMA techniques may be applied to allocate different time slots to each unit.

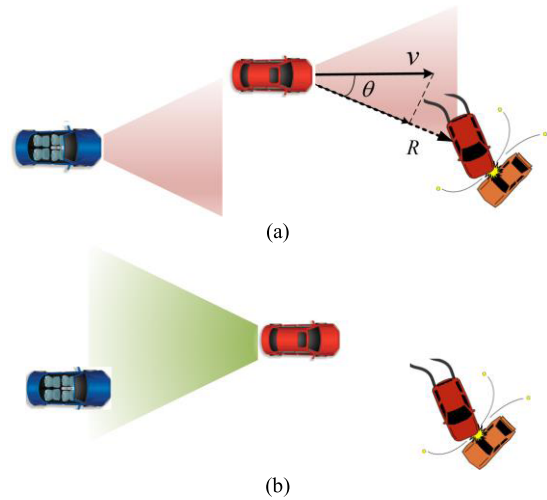As a radar, the system can estimate the position of either a mobile or stationary object. Furthermore, echo signal arrives at receiver with a frequency difference (beat frequency) associated with time delay that corresponds to object's range and velocity of motion with respect to receiver's reference point. Since the waveform is a combination of the triangle FMCW and single frequency Doppler radar, the information may be obtained through similar analysis of these waveforms [21]. Range (R) and velocity (v) can be obtained from beat frequencies (f_b) through the following expressions:

$$\begin{cases} f_{bu} = \dfrac{2\Gamma R}{c_0} + \dfrac{2f_2 v \cos\theta}{c_0} \\[2mm] f_{bd} = -\dfrac{2\Gamma R}{c_0} + \dfrac{2f_2 v \cos\theta}{c_0} \\[2mm] f_{bc} = \dfrac{2f_2 v \cos\theta}{c_0} \end{cases} \qquad (2)$$

where θ is the angular position of target that equals the angle of arrival (AOA) of the echo beam. The sign of the velocity of an approaching target is assumed to be negative and vice versa.

In order to make the beat signal to convey information about AOA, the echo signal can be received with a phase difference ($\Delta\varphi$) by two separate elements of receiver (Rx) antenna. For this RadCom system, the low-cost two-elements receiving array technique [22] is adopted, as opposed to conventional beam steering technique that demands for several receiver channels [23].

In a coherent FMCW radar, $\Delta\varphi$ can be preserved even after down conversion, provided that the RF paths of two branches are identical in terms of electrical length. This phase difference appears in beat signals and can readily be estimated after frequency transform. With the assumption of an infinite integration time, AOA and subsequently angular position of nth detected object can be found through the following

expressions:

$$\begin{cases} S_{bi}^2(f) = S_{bi}^1(f)e^{j\Delta\varphi(f)} = \sum_{k=1}^{N} \delta(f - f_k)e^{j\Delta\varphi(f_k)} \\ \theta_k = \sin^{-1}(\dfrac{\Delta\varphi_k}{2\pi d/\lambda}) = \sin^{-1}(\dfrac{\psi_{bi}^2 - \psi_{bi}^1}{2\pi d/\lambda}) \\ i = u, c, d \end{cases} \quad (3)$$

where d is the spacing between antenna elements, and N is the number of detected objects. ψ_b^1 and ψ_b^2 are the phase of the detected beat signals from the first and second channels, respectively. Unlike the time domain correlation of received signals from Rx antenna with two separate elements, the estimation of angle through (3) allows discrimination of several targets in angle, provided that the beat signals are discriminated in PSD spectrum.

III. TFMCW RADAR SIGNAL ANALYSIS

The radar cycle in the in-time-domain integrated RadCom system can be reconfigurable, depending on the scenario of operation. Furthermore, the operational signal may be configured to either triangle or trapezoidal FMCW. The latter one is the preferable solution in the context of RadCom systems as it may outweigh especially in multi-target environments. We have re-examined the fundamental features of this radar signal throughout simulations in terms of 1) ambiguity intervals, 2) multi-target detection and 3) estimation accuracy. The results of this study are discussed concisely next, which brings in a quick reference for this multi-functional transceiver design.

A. AMBIGUITY INTERVALS

In order to determine the essential type of demodulation of the radar signal, whether quadrature or in-phase, the range of variation of beat frequencies should be studied. Fig. 3 shows all possible values of the beat frequencies along with the variation of the range from 0 m to 100 m and the velocity from −250 km/h to 250 km/h.

The beat frequencies which are obtained from (2) experience both negative and positive signs. Hence, the calculations of the range and velocity must be done with the true sign in order to avoid any ambiguity. This requires obtaining the spectrum of the beat signals using the complex data that may be obtained through quadrature demodulation via de-chirping mixer. Also, the quadrature component of the received in-phase signal can be obtained through its Hilbert transformed signal [24]. Replacing the quadrature demodulator with the in-phase mixer reduces the complexity of the radar RF front-end but at the expense of a heavier computation burden.

B. MULTI-TARGET DETECTION

FMCW radars may readily estimate the range and the relative velocity of a single detected target through a pair of up or down-chirp beat signals. However, this estimation gets complicated when several targets exist as any pair of the
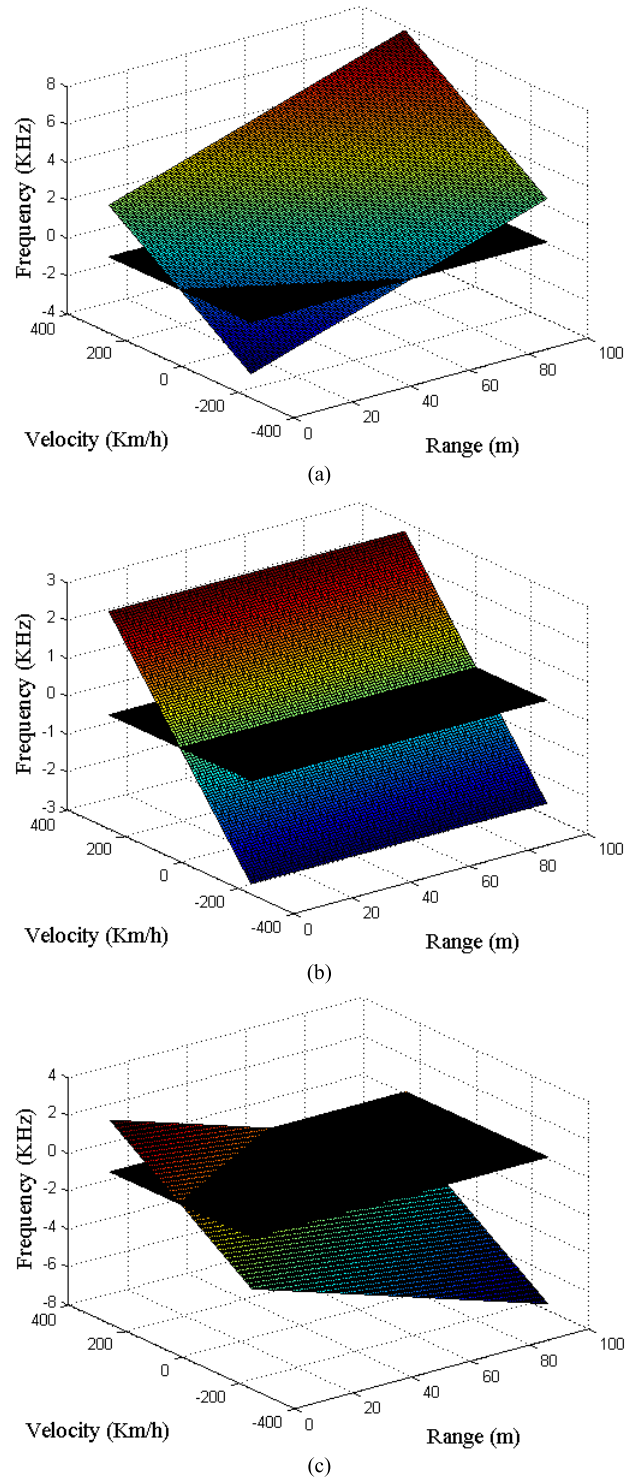

(a)

(b)

(c)

FIGURE 3. Beat frequencies along with the variation of range and velocity; Sign of the beat frequencies must be respected as none of them has a single sign in the whole range. The color differences from red to blue highlights the differences in calculated values of beat frequencies from maximum to minimum ones. (a) Up-chirp beat. (b) Constant beat. (c) Down-chirp beat.

beat signals is possible that may yield ghost target detection or incorrect parameter estimation. This problem can be solved by repeating triangle FMCW with different rates or

sending an unmodulated signal besides up-chirp and down-chirp [29], [30], [32]. A similar technique may be applied for this RadCom scheme.
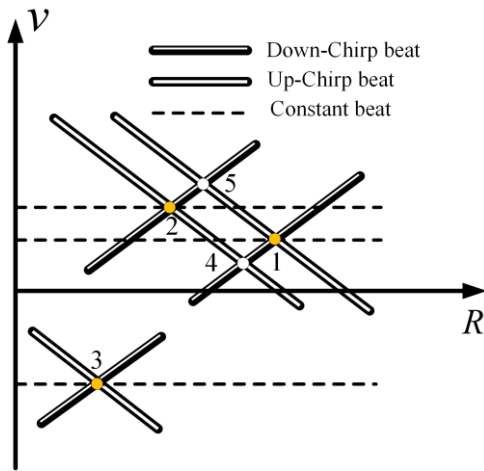

FIGURE 4. V-R diagram from a TFMCW radar; Nodes 4 and 5 are ghost targets which may not be distinguished from real targets if the constant beats do not exist. Unlike targets 1 and 2, target 3 is approaching the radar.

Fig. 4 shows the Range-Velocity diagram of TFMCW radar when detecting three beat signals. This plot can be obtained by reforming (2) as

$$\begin{cases} v_u = \alpha f_{bu} - \alpha\beta R \\ v_d = \alpha f_{bd} + \alpha\beta R \\ v_c = \alpha f_{bc} \end{cases} \quad (4)$$

where $\alpha = c_0/(2f_2cos\theta)$ and $\beta = 2\Gamma/c_0$. Parameter estimation should be obviously made at the intersection points in the R-V diagram which may yield ghost target detection in triangle FMCW radars. In the typical example of Fig. 4, one can see that the radar system may detect two extra targets mistakenly given using only up and down chirp beat signals.

In order to find the correct group of beat signals, a vector of beat frequencies can be made for each up-chirp beat frequency using all constant beat frequencies by

$$\bar{P}_{di} = 2\bar{f}_c - f_{ui} \quad (5)$$

where, f_{ui} is the ith beat frequency in the up-chirp time slot, $\bar{f}_c$ is the vector of all detected constant beat frequencies and $\bar{P}_{di}$ is a vector of all possible down-chirp beat frequencies. For each up-chirp beat frequency one vector of $\bar{P}_d$ should be made. Then each element of $\bar{P}_d$ that agrees with the one of the true detected down beat frequencies must be used with the associated constant and up-chirp beat frequencies in group for further calculations. The technique is explained further in the following example.

Fig. 5 shows the multi-target scenario with three moving targets which is simulated in Matlab [27]. The radar signal after de-chirping mixer is simulated [24] and the chirp time slot is selected long enough so that it covers the maximum unambiguous range as well as the velocity resolution,
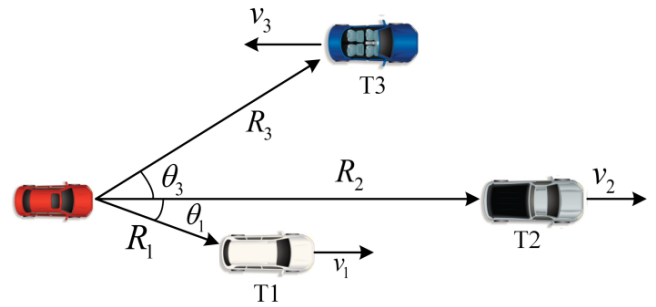

FIGURE 5. Multi-target simulation scenario; R1 = 45 m, R2 = 100 m, R3 = 60 m, V1 = 70 km/h, V2 = 150 km/h, V3 = −30 km/h, θ_1 = 23°, θ_3 = 40° and θ_2 = 0°.

i.e. maximum value between $(10 \times 2 \times R_{max})/c$ and $\lambda/(2 \times V_{res})$.
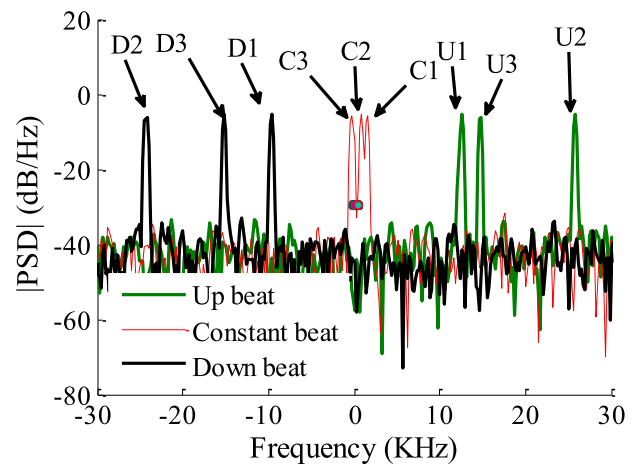

FIGURE 6. PSD of the detected beat signals from simulation in Matlab. Three beat frequencies are detected at each time slot. D, C and U denote the peaks in down-chirp, constant and up-chirp time slots, respectively. In multi-target scenario, all peaks apear together and it is unknown which peak pertains to which target which makes correct target detection complicated.

The maxima above the threshold in the periodogram shown in Fig. 6 are detected in each time slot and three vectors are made including the detected beat frequencies. It is still not clear how many targets exist and also which group of beat frequencies must be used for calculations. Using (5), three vectors of $\bar{P}_{di}$ are made, and then compared with the down beat frequencies. Fig. 7(a) shows p1, p2 and p3 as the first, second and third elements of each of the vector of $\bar{P}_{di}$.

One can observe that three targets are detected and the appropriate group of beat frequencies for each target is found as it is shown in Fig. 7(b). The calculation results are listed in Table I. One can see that the targets are detected correctly. The importance of the angle detection in true estimation of the real target's velocity is also noticeable.

C. ESTIMATION ACCURACY
In order to find out the minimum required SNR of the received beat signals for estimations of the range, velocity and
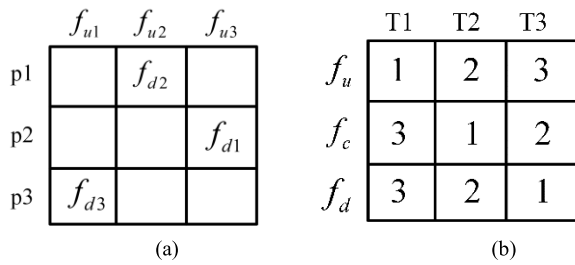
FIGURE 7. Beat frequency pairing for multi-target detection; (a) Table of comparison of $\bar{P}_{di}$ with f_d; three matches are found, hence three targets exist. (b) Group of beat frequencies that should be used for calculations; the numbers indicate the indices of the detected beat frequency vectors.

**TABLE 1.** Multi-target simulation results.

Simulation Parameters			
Target	**Range (m)**	**Angle (°)**	**Velocity (km/h)**
T1	45	23	150
T2	100	0	70
T3	60	40	-30
Simulation Results			
Target	**Range (m)**	**Angle (°)**	**Velocity (km/h)**
			v	$v/\cos(\theta)$
T1	45	23.265	137.872	150.051
T2	100	0.131	68.936	68.936
T3	60	-39.917	-22.979	-29.960

angle with enough accuracy, a statistical analysis is carried out with a few set of simulations of a scenario with only one point target in Matlab. This preliminary information can be used in transceiver design.

In practice, the SNR varies mainly because of the changes in signal level for targets with different RCS in different distances if the background noise level remains constant. However, to keep the analysis independent of any additional processing technique for detection, the signal level is assumed to be constant, but the noise level is tuned to change the SNR. Signal detection occurs when the signal in PSD crosses the threshold level [29].

Fig. 8 shows the standard deviation (STD) of error in range and velocity estimation for different values of SNR and threshold to mean noise level. One can observe that the main reason of error in range estimation is the wrong detection and when a correct detection happens (with threshold level around 12 dB) the calculation would be correct and remains constant for a range of SNR. The STDs of errors in range and velocity converge to 0.488 m and 0.63 m/s which are half of the estimation error in range (e_r) and velocity (e_v), respectively. These values correspond to the frequency resolution of PSD with selected FFT length (N), i.e $e_r/2 = c_a f_s T_c/(4N\text{BW})$ and $e_v/2 = c_a f_s/(4Nf_c)$ where f_s is the sampling frequency and BW denotes the sweeping frequency bandwidth.

The minimum threshold level of around 12 dB from our simulations is associated to the false alarm rate under
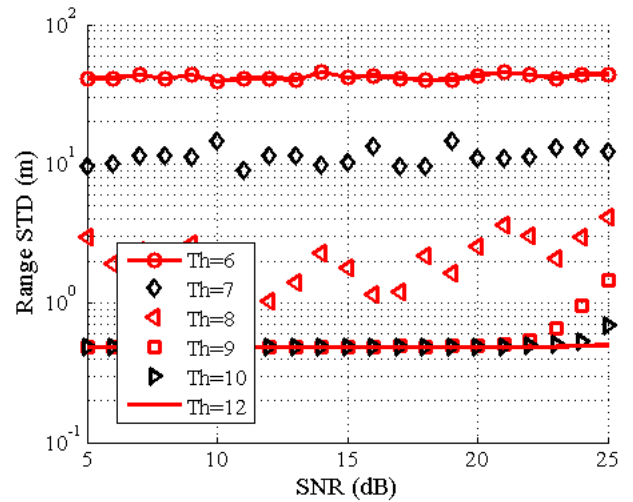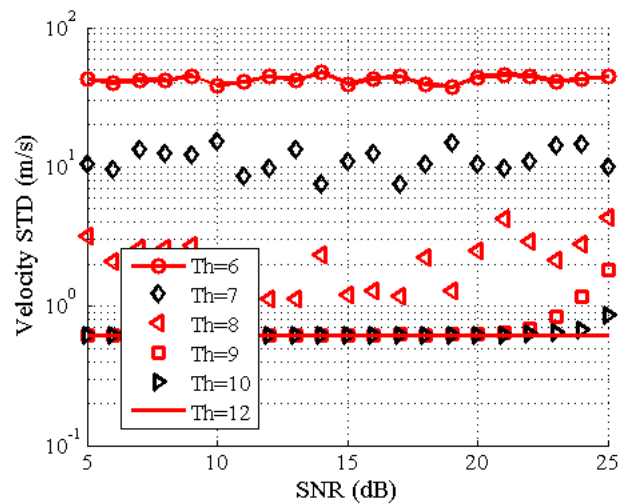
FIGURE 8. Variation of estimation error as a function of threshold to noise level and SNR in simulation via Matlab; The chirp length is selected to be 20 ms that sweeps 150 MHz bandwidth around 5.8 GHz. Beat frequencies occur in the middle of the two adjacent spectrum resolution points. Sampling frequency is 50 kHz and the STD is obtained out of 10000 runs for each point. (a) Standard deviation of the range estimation. (b) Standard deviation of the velocity estimation.

10^{-6} that requires a threshold-to-noise ratio (*TNR*) of at least 11.4 dB from $TNR = \ln(1/P_{fa})$ [32].

For practical applications and in the presence of clutter or multiple targets, appropriate constant-false-alarm-rate (CFAR) technique must be applied [33]. Range operational curve (ROC) of FMCW radar based on target detection from periodogram may also be obtained, using the same analysis [29].

The same analysis is carried out for angle estimation when the threshold to noise ratio is considered to be identical to SNR. Two different cases are considered, i.e., beat frequency occurs in an integer or fractional multiplication of frequency resolution. The STD results demonstrated in Fig. 9, confirm that the accuracy of angle estimation improves with
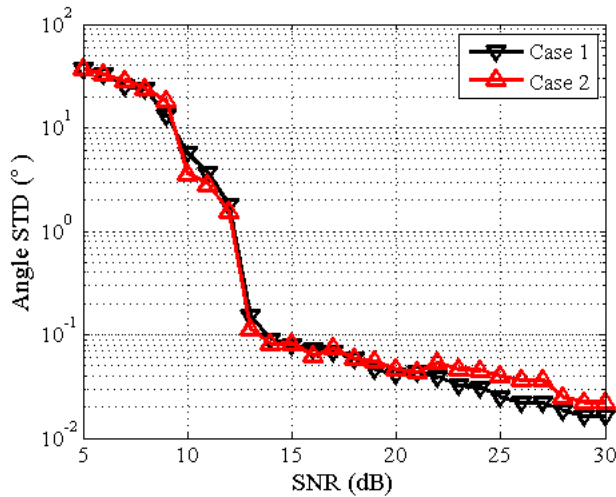
FIGURE 9. Variation of angle estimation error as a function of threshold to noise level or SNR in simulation via Matlab; Case 1: Beat frequencies occur at the spectrum resolution points. Case 2: Beat frequencies occur in the middle of the two adjacent spectrum resolution points.

TABLE 2. System specification.

Mode	Specification	Values
	Frequency band	5725-5875 MHz
	Channel bandwidth	150 MHz
	Max. power (EIRP)	41 dBm
	Min. & Max. detectable range	1 m & 100 m
	Range resolution	1 m
	Max. detectable velocity	250 km/h (64.44 m/s)
Radar	Velocity resolution	5 km/h (1.29 m/s)
	Angular area coverage	±45°
	False alarm rate	1e-6
	Probability of detection	0.9
	Max. communication range	1000 m
Radio	Max. data rate	75 Mbps
	Bit error rate for BPSK	1e-6

the larger values of SNR for both cases as it depends directly on the phase.

Abrupt drop of STD occurs at SNR and also TNR of around 13 dB where a false detection would not take place. Consequently, a minimum SNR value of around 12 dB to 15 dB should be considered if correct estimation of all three parameters of range, velocity and angle is desired.

IV. SYSTEM ARCHITECTURE AND ANALYSIS

A. EXPERIMENTAL RadCom SYSTEM SPECIFICATIONS

According to the FCC rules [31] and desired specifications of middle range automotive radar [23] and mobile radio for DSRC applications, we have defined the whole system operational specification that is listed in Table 2. 150 MHz between 5.725-5.875 GHz around DSRC band is considered for prototyping in order to have a desired range resolution which is in inverse relationship with bandwidth i.e., $\Delta R = c_o/(2BW)$.

B. RADAR – RADIO INCOMPATIBILITIES

Apart from the differences in the operational signal, the design and performance incompatibilities between radar

TABLE 3. Link budget analysis.

Characteristics	Radar Mode	Radio Mode
Operational Range	100 m	1000 m
Total Cycle	60 ms	20 ms
Receiver video Bandwidth	400 kHz	50 MHz
Transmitting Power	22.34 dBm	22.34 dBm
Transmitter's Antenna Gain	19 dBi	19 dBi
Friis Path Loss	175.42 dB	107.71 dB
Radar Cross Section Gain	36.83 dB	----
Receiver's Antenna Gain	7 dBi	7 dBi
Signal Power at the Receiver Input	-90.25 dBm	-59.37 dBm
Thermal Noise Power at the Rx Input	-117.98 dBm	-96.85 dBm
SNR at the Receiver Input	27.73 dB	37.48 dB
Receiver Noise Figure	7 dB	7 dB
SNR at the Receiver Output	20.73 dB	30.14 dB
Roll-off Factor	----	1
Data Rate-BPSK	----	25 Mbps
E_b/N_o	----	33.14 dB
Required SNR (E_b/N_o in Radio mode)	15 dB	10.5 dB
Link Margin	5.73 dB	22.64 dB

and radio systems are indeed the main factors that make a RadCom transceiver design not straight forward. These incompatibilities come into view upon initial budget analysis, which is summarized in Table 3. The following observations in Table 3 are worthwhile to mention.

First, the required video bandwidth in relation with noise bandwidth for radar mode is much less than that in radio mode. Furthermore, for a radio system, the required SNR originates from the desired BER which depends on the energy-per-bit to noise-power-spectral-density ratio (E_b/N_0). It is related to SNR by

$$ SNR = \frac{R_s}{BW_{radio}} \times \frac{E_s}{N_0} = \frac{\log_2 M}{\beta + 1} \times \frac{E_b}{N_0} \qquad (6) $$

where BW_{radio} is the bandwidth of radio signal which depends on the roll-off factor (β) of the Nyquist filter, and the symbol rate R_s. M denotes the order of modulation which is 4 for QPSK as an example [34].

In stretch processing or "de-ramping" the energy of the signal would remain the same before and after the process. However, it is congested in a narrow temporal pulse, i.e, ($T_p = 1/BW$), and hence it is more than the one before compression. This processing gain is the chirp's "time-bandwidth" product indeed, i.e. T_cBW. However, the random noise power does not change as it is not correlated to the transmitted signal. Hence, the SNR would change and this gain in SNR may be considered in radar equation. Alternatively, this can be viewed as the noise power in the beat signal is less than the one in the chirp as in

$$ SNR = \frac{P_b}{P_n} = \frac{P_s \times T_c \times BW}{N_0 BW} = \frac{P_s}{N_0 \times \frac{1}{T_c}} \qquad (7) $$

where P_b and P_s are the beat and chirp signal power, respectively [35], [36]. Hence, the receiver noise bandwidth in radar mode may be assumed to be the beat signal video bandwidth which can be determined based on the maximum detectable
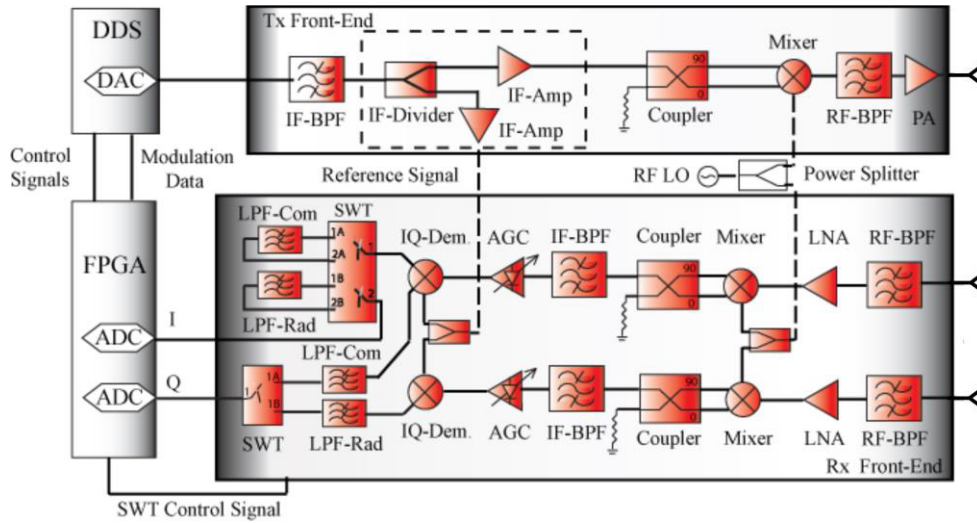
FIGURE 10. Proposed transceiver architecture.

range and velocity and also the chirp slope. The duration of the chirp-slot (T_c) should be selected large enough in order to have the desired resolution in velocity measurement ($\lambda/(2T_c)$). Thus, the radar receiver bandwidth at the output can be much smaller than the one of radio receiver and should be controlled in order to suppress the excessive noise in radar mode.

Second, the propagation channel behaves differently in terms of path loss. In fact, the received radar signal power can be viewed as

$$P_r^{Rad} = P_t G_t G_r G_{rcs} P_{loss}^{Rad} = P_t G_t G_r (\frac{4\pi\sigma}{\lambda^2})(\frac{\lambda^2}{(4\pi)^2 R^2})^2 \tag{8}$$

where P_t is the transmitted power, G_t is the Tx antenna gain, G_r is the Rx antenna gain, G_{rcs} is the RCS gain and P_{loss}^{Rad} is the path loss in radar mode. Received power in communication mode (P_r^{Com}) can be obtained from (8) by eliminating G_{rcs} and taking the root-square of P_{loss}^{Rad} as path loss of communication channel. From this standpoint, the received radar signal power would be much less than the radio one given the same transmitter output power. The RCS gain may vary among the ITS related objects, but in this initial calculation σ is considered to be unity, i.e. $\sigma = 1$, which yields RCS gain of 36.82 dB for a non-fluctuating target.

The radio signal level should be fixed at a specific value before the symbol decision-making device, therefore using an AGC (automatic gain control) loop in the receiver block is a common solution. On the other hand, the radar signal level varies from -10 dBm to -90 dBm for a typical target with $\sigma = 1$. The difference can be even larger when large and small objects are detected at short and long distances, respectively. This high dynamic range requires an excellent linearity of both receiver front-end and the ADC. If the dynamic range of the ADC is not sufficient (72 dB for our 12-bit ADC), an AGC loop can be used for

desensitizing the receiver through attenuating the large returned signals.

C. TRANSCEIVER ARCHITECTURE

According to all the above mentioned observations related to system requirements, a heterodyne transceiver architecture is proposed, as shown in Fig. 10 which is explained next.

The combination of DDS (AD9858) and FPGA (Altera-Stratix) boards in the back-end forms a software-defined signal generator which is capable of reconfiguration. The FPGA is able to control the DDS for either frequency sweeping or phase shifting in an absolute timing manner with output carrier at intermediate frequency (IF).

In the transmitter front-end, an active in-phase divider is positioned between the low-pass filter (LPF) and the up-convertor. Using this divider a branch of the IF signal is taken as a reference signal to be used as the carrier of the Quadrature demodulator in receiver in radar mode and also in radio mode when receiving signal from other unit. The combination of 90° hybrid coupler and I-Q mixer forms a single side-band (SSB) up-convertor. Heterodyne products are first filtered out by a band-pass filter (BPF) and then the desired RF component is amplified in power amplifier (PA) block before going to the Tx-antenna.

The Rx-antenna is a low-gain antenna and is separated from the transmitting antenna to have a better isolation. This antenna must capture two samples of the arriving beam with a phase difference that represents the AOA.

The receiver front-end consists of two identical channels, each connecting to a single element on Rx-antenna. The received signal in each channel is amplified in low-noise amplifier (LNA) block and then down-converted in frequency by image rejection mixing. A wide range of fluctuations at the IF signal level can be compensated by an AGC loop. Thereby, two quadrature demodulators are fed at a fixed signal level.
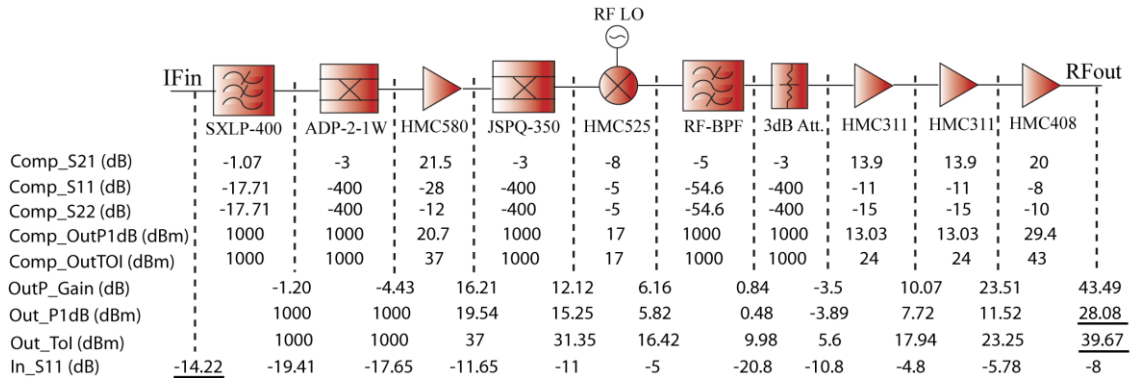
	SXLP-400	ADP-2-1W	HMC580	JSPQ-350	HMC525	RF-BPF	3dB Att.	HMC311	HMC311	HMC408
Comp_S21 (dB)	-1.07	-3	21.5	-3	-8	-5	-3	13.9	13.9	20
Comp_S11 (dB)	-17.71	-400	-28	-400	-5	-54.6	-400	-11	-11	-8
Comp_S22 (dB)	-17.71	-400	-12	-400	-5	-54.6	-400	-15	-15	-10
Comp_OutP1dB (dBm)	1000	1000	20.7	1000	17	1000	1000	13.03	13.03	29.4
Comp_OutTOI (dBm)	1000	1000	37	1000	17	1000	1000	24	24	43
OutP_Gain (dB)		-1.20	-4.43	16.21	12.12	6.16	0.84	-3.5	10.07	23.51	43.49
Out_P1dB (dBm)		1000	1000	19.54	15.25	5.82	0.48	-3.89	7.72	11.52	28.08
Out_Tol (dBm)		1000	1000	37	31.35	16.42	9.98	5.6	17.94	23.25	39.67
In_S11 (dB)	-14.22	-19.41	-17.65	-11.65	-11	-5	-20.8	-10.8	-4.8	-5.78	-8

FIGURE 11. Chain budget simulation of Tx block.

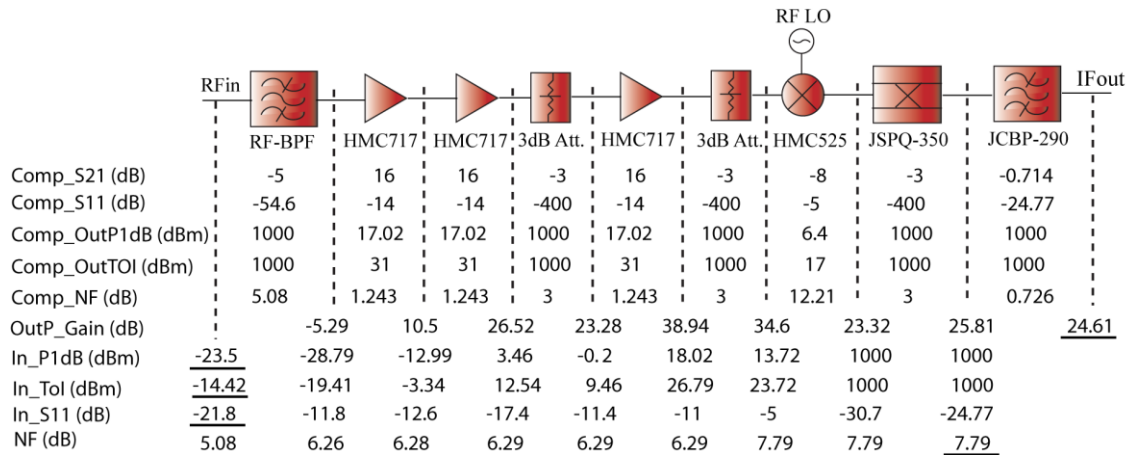|	RF-BPF	HMC717	HMC717	3dB Att.	HMC717	3dB Att.	HMC525	JSPQ-350	JCBP-290
Comp_S21 (dB)	-5	16	16	-3	16	-3	-8	-3	-0.714
Comp_S11 (dB)	-54.6	-14	-14	-400	-14	-400	-5	-400	-24.77
Comp_OutP1dB (dBm)	1000	17.02	17.02	1000	17.02	1000	6.4	1000	1000
Comp_OutTOI (dBm)	1000	31	31	1000	31	1000	17	1000	1000
Comp_NF (dB)	5.08	1.243	1.243	3	1.243	3	12.21	3	0.726
OutP_Gain (dB)		-5.29	10.5	26.52	23.28	38.94	34.6	23.32	25.81	24.61
In_P1dB (dBm)	-23.5	-28.79	-12.99	3.46	-0.2	18.02	13.72	1000	1000
In_Tol (dBm)	-14.42	-19.41	-3.34	12.54	9.46	26.79	23.72	1000	1000
In_S11 (dB)	-21.8	-11.8	-12.6	-17.4	-11.4	-11	-5	-30.7	-24.77
NF (dB)	5.08	6.26	6.28	6.29	6.29	6.29	7.79	7.79	7.79

FIGURE 12. Chain budget simulation of down-convertor core in Rx block.

Switching technique is used for three purposes. First, it helps preserve the sensitivity of the receiver in two modes by controlling the bandwidth. Second, the quadrature mixers are shared between two channels in two modes. Indeed, both quadrature (Q) and in-phase (I) components of a single demodulator are allocated to the communication signal whereas at least one component from each demodulator is required for eliciting all desired radar information. And third, the required number of ADCs is minimized by multiplexing I and Q components of the two channels. In radio mode, I and Q components of one channel go to ADC to be sampled, whereas in the radar mode at least one component from each channel is required and therefore out of four, only two of them, i.e., one from each mixer, go to ADC to be sampled and further processed. This does not disturb the necessity of coherent and simultaneous radar signal receiving from the two channels.

V. SIMULATIONS
A. RF CIRCUIT SIMULATION
Based on the above analysis and the proposed architecture, both transmitter and receiver circuitries are designed using commercial off-the-shelf components. With the purpose of optimization, the circuits are carefully simulated via Harmonic-Balance (HB) and Chain-Budget platforms in the commercial simulation package of Advanced Design Systems (ADS) [37]. In these sets of simulation, either S- or X-parameters of RF chips, provided by manufacturers in datasheets, are used for characterization of the corresponding simulation components. Two design aspects are considered for optimum chip selection and configuration.

First, the minimum number of amplifiers is used and second, the interference from spurs is minimized by moving third-order-intercept (TOI) point away from 1dB-compression point (P1dB). Fig. 11 shows the up-convertor block accompanying the results of a chain-budget analysis. With nominal input power of −15 dBm, an input matching of around −14 dB is achieved and the TOI point is also around 11 dB higher than the compression point.

Fig. 12 shows the down-convertor block with all building components. A perfect input matching of 21.8 dB and TOI of 10.2 dBm at the output is achieved that is around 10 dB larger than the compression point.

The noise figure (NF) of 7.79 dB is slightly more than the specified one in the link budget analysis. This is due to the loss of the RF BPF, which is considered to be 5 dB in simulation. The same filter with 1 dB bandwidth of 150 MHz is used in the up-convertor for suppressing the LO, which is only 225 MHz away from the center frequency of 5.8 GHz. Given at least 20 dB rejection at LO frequency, 5 dB loss could be inevitably anticipated in practice.
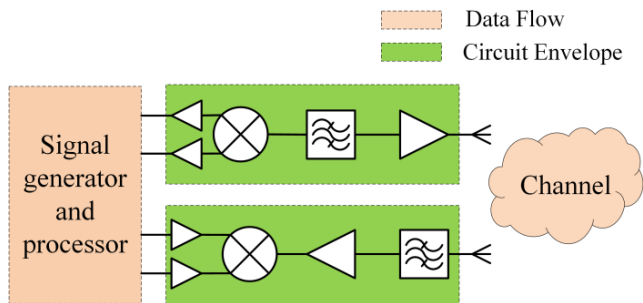

FIGURE 13. Block diagram of multilayer simulation at system level via Ptolemy simulator in ADS package. The characteristics of each off-the-shelf component in both Rx and Tx blocks are taken from datasheets and the propagation is modeled in a free-space channel with AWGN. The signal flow in RF circuit and propagation channel is controlled by the Circuit-Envelope and Dataflow simulators, respectively.

B. SYSTEM LEVEL SIMULATION

In order to investigate a proper operation of the whole system, a series of simulations are carried out at the system-level via Ptolemy simulator in ADS. In this platform, various aspects from nonlinear effects in RF circuitry to fading in propagation channel or even sampling noise in ADC can be taken into account. Fig. 13 shows the block diagram of this type of multi-layer co-simulation. Indeed, the signal flow in RF circuits is controlled by the Circuit-Envelope simulator at the bottom layer while Dataflow simulator controls all signal processing as well as signal flow in propagation channel at the top layer. The desired modulated signal in (1) is generated by a combination of discrete signal processing DSP blocks in discrete time domain and then transformed to continuous time domain. For instance, the up-chirp signal that enters the bottom layer is made in the form of,

$$S_{upchirp}(t) = Ae^{j2\pi(0.5\Gamma(T_{step}^2 n^2)+f_1 T_{step} n)} \times e^{j2\pi f_c t} \quad (9)$$

where f_c is the carrier, n is the discrete time index and T_{step} is the simulation time step. Note that the chirp slop and the chirp starting frequency are denoted by ΓT_{step}^2 and $f_1 T_{step}$, respectively.

C. SIMULATION RESULTS OF RADAR MODE

Fig. 14(a) shows the spectrum of a radar signal arriving at the receiver input. The AWGN channel is configured to resemble the existence of a target which is 100 m away from the receiver.

Beat signals are sampled by the ADC blocks at sampling rate of 10 MHz and then transformed to frequency domain
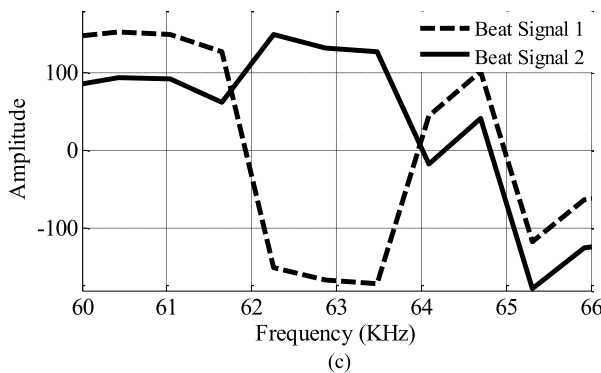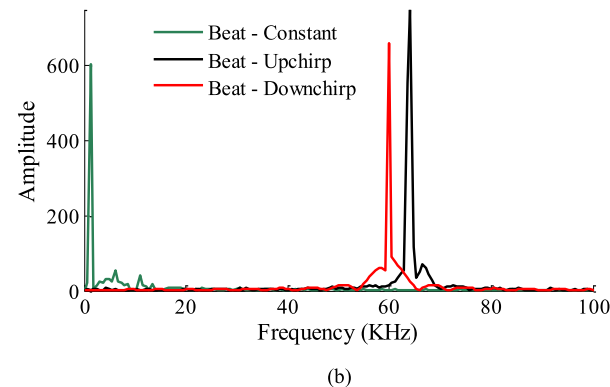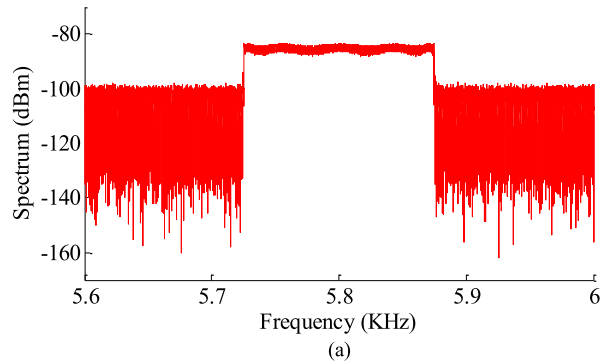

FIGURE 14. System simulation when operating in radar mode; The distance of the target from Rx antenna and it's angular position is 100 m and 20°, respectively. The AOA can be obtained from (3), using the phase difference of beat signals at the peak frequency. (a) Power spectrum of the radar signal at the receiver input. (b) Spectrum of the detected beat signals. (c) Phase of the Up-chirp beat signals after DFT; M2 = −17.508, M1 = 44.137.

through 8192-points discrete Fourier transform (DFT) algorithm with around 1.22 kHz frequency resolution. Doppler-Effect is taken into account through appropriate I-Q frequency up or down conversion with the corresponding Doppler frequency. Amplitude and phase of the resulting signals are shown in Fig. 12(b) and (c).

The existence of a peak in amplitude notifies the detection of an object at a distance that corresponds to the frequency in which peak appears. For estimating the AOA, the phase difference should also be read at this frequency. The results are summarized in Table 4. Note that the deviation in

TABLE 4. System simulation results for radio mode.

Simulation Parameters		
Chirp duration	1.6384 ms	
Center freq.	5.8 GHz	
Bandwidth	150 MHz	
SNR	15 dB	
Sampling freq.	10 MHz	
DFT length	8192	
Number of samples	0.9*Fs*Ts	
Simulation Scenario	**# 1**	**# 2**
Target's range	100 m	100 m
Target's velocity	119 km/h	119 km/h
Radar velocity	0 km/h	0 km/h
Target's angle	20°	20°
Relative velocity	112 km/h	112 km/h
Direction	Receding	Approaching
Simulation Results	**# 1**	**# 2**
f_{bu}	64.089 kHz	61.645 kHz
f_{bd}	61.645 kHz	64.089 kHz
f_{bc}	1.2207 kHz	1.2207 kHz
R	103 m	103 m
v	119 km/h	119 km/h
θ	20.027°	20.01°

simulation results is mainly attributed to the intrinsic time delay in RF circuitry at the bottom layer and also the low resolution of the DFT in simulation.
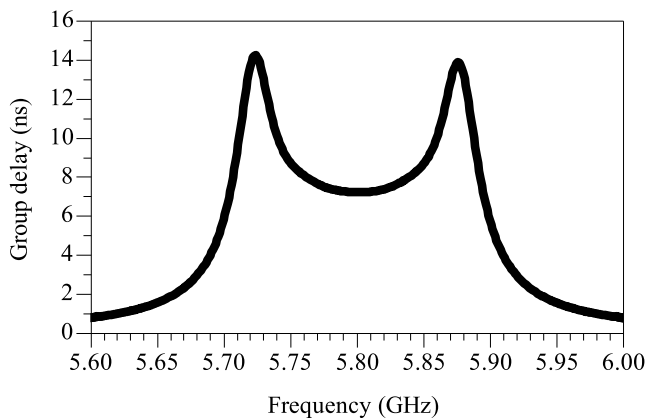
FIGURE 15. Group delay of the RF BPF which is used in both Tx and Rx blocks for simulation in ADS; In-band group delay of around 9 ns causes a constant error in parameter estimations.

Fig. 15 shows the group delay of the employed band-pass filter (BPF) both at the transmitter output and the receiver input. The received signal at the de-chirping mixer experiences this delay twice which yields a constant offset in range measurement. This is expected to occur in practice and therefore, the system requires calibration.

The simulation is repeated with the BPFs bypassed and the obtained up, down and constant beat frequencies
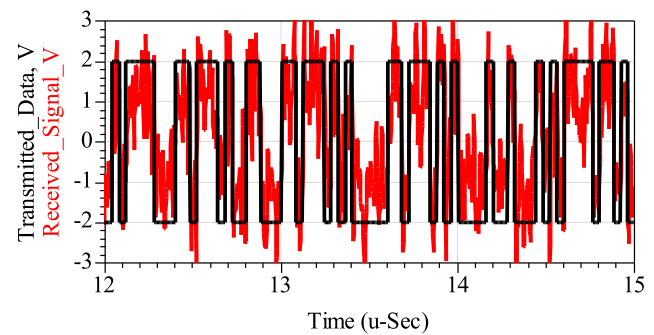
were 62.255289 kHz, 1.202703 kHz and 59.814453 kHz, respectively. Consequently, the estimated range was exactly 100 m.

D. SIMULATION RESULTS OF COMMUNICATION MODE

For system simulation in radio mode, the carrier in radio cycle is modulated by BPSK scheme.
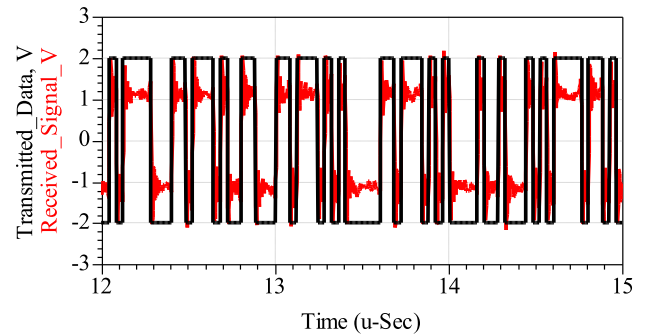
(a)

(b)

FIGURE 16. System-level simulation results when operating in communication mode. (a) Eb/N0=12dB. (b) Eb/N0=3dB.

Depending on a desired E_b/N_0, the noise power spectral density of the propagation channel can be controlled by $10 log_{10} \left(\frac{P \times T_s}{log_2 M} \right) - \frac{E_b}{N_0}$, where P is the signal power at the output of the Tx antenna, T_s is the symbol duration and M denotes the order of modulation. Fig. 16 shows the results of simulation for two different cases of $E_b/N_0 = 12$ dB and 3 dB, where we can observe the system capability to communicate with a high data rate.

VI. PROTOTYPING AND MEASUREMENTS

All individual circuits in the front-end of the low-frequency demonstrator of our proposed system are fabricated in-house using low-cost printed circuit board (PCB) process on substrate Rogers-4350B with thickness of 0.508 mm. Grounded coplanar waveguide (CPWG) topology is preferred as transmission line in the PCB layout due to its low radiation loss and leakage as well as enhanced isolation because of a larger ground plane between RF lines. Upon the evaluation of each circuit, all are assembled in two separate aluminum housings as transmitter (Tx) and receiver (Rx) blocks considering
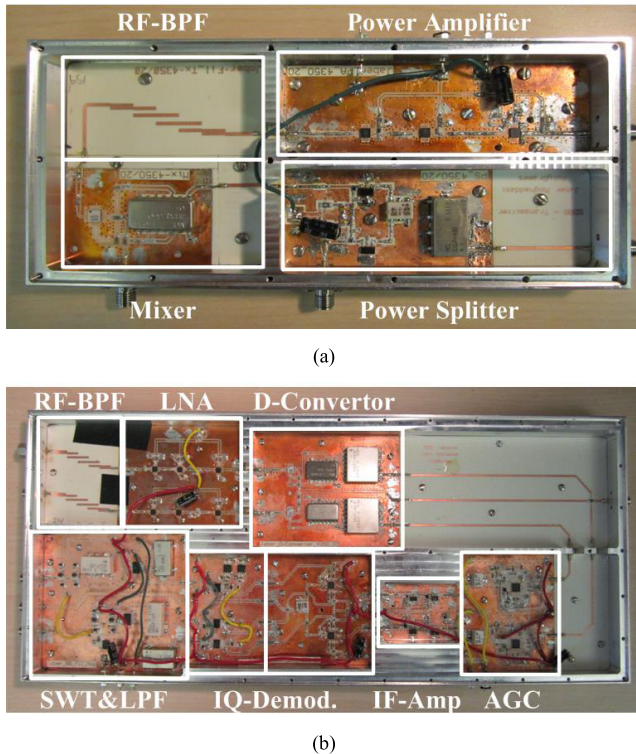
(a)

(b)

FIGURE 17. Prototyped building blocks of front-end. (a) Transmitter block. (b) Receiver block.

electromagnetic compatibility issues. Fig. 17 shows the Tx and Rx blocks indicating each functional unit.

The performance of the proposed transceiver is evaluated through different tests in either individual circuit or system level and some measurement results are presented next:

A. Tx BLOCK

In order to test the performance of the proposed signal transmitting unit in terms of linearity, output of the transmitter block is probed using DSO and then analyzed further in VSA. Our signal source is configured at radio mode and generates a BPSK modulated signal by 25 Mbps pseudorandom bit sequence (PRBS) with a maximum length of 2^{11}-1.

The measured error vector magnitude (EVM) is around 2.25%rms with IQ phase error of 512.88 mdeg, magnitude error of 2.068%rms and IQ-offset of −40 dB. In addition, the parameter that can evaluate the linearity of the transmitter front-end is the error vector spectrum. Furthermore, small in-band inter-modulation spurs that may not appear in spectrum of the demodulated signal can show up in error vector spectrum and thereby the magnitude and frequency offset of the spurs can be observed [38]. The cumulative graph of error vector spectrum of the demodulated carrier is shown in Fig. 18. Inexistence of any in-band spurs proves that up-convertor and PA units are highly linear.

B. DOWN-CONVERTOR BLOCK

Down-convertor block which includes two channels of RF BPF, LNA and image rejection mixer is examined for
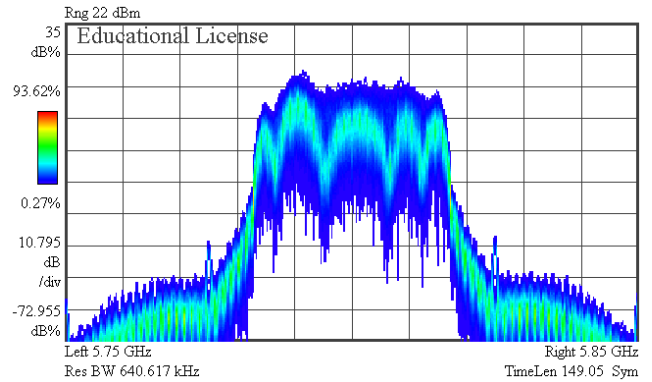

FIGURE 18. Cumulative graph of EVM spectrum of the signal at the output of Tx block. Error vector spectrum can monitor the small in-band intermodulation spurs that may not appear in the spectrum of the signal [38]. This shows that the Tx block is highly linear as no spurs exist in band and the ones at corners are around 50 dB lower from the in-band signal level.

NF and gain by NF analyzer (Agilent N8975A) and hot noise source (Agilent SNS-4002A). Measured results of both channels are shown in Fig. 19.
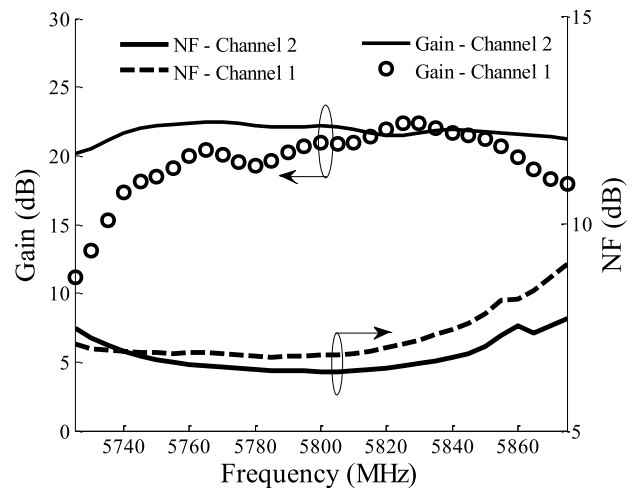

FIGURE 19. Gain and NF of both branches of down-convertor block measured by NF analyzer (Agilent N8975A) and hot noise source (Agilent SNS-4002A).

It can be seen that NF for both channels is almost around 7 dB as was anticipated according to chain budget simulations. Gain is also around 22 dB that is 2 dB less than the HB simulation results. This attributes to the loss in PCB and connections between three circuits. The variation in measured gain of channel-1 is caused by mismatch and cross-coupling in PCB.

C. AGC LOOP

The Principal cores of an AGC loop are a variable gain amplifier (VGA), an RF detector and a directional coupler. Among three different types of RF detectors, logarithmic detector as opposed to RMS and envelope detector gives the fastest response to recover from large abrupt decreases in

signal level thanks to the steep slope of logarithmic curve for low inputs [39], [40]. This features the AGC loop with a high response time and therefore it is appropriate for the RadCom system that experiences large collapse in input power transferring from communication mode to radar mode. For our system demonstrator, this loop is realized by a 7dB directional coupler, two IF amplifiers (GVA-82 and GVA-62) and an IC package (HMC992LP5E) which houses VGA and log-detector cores. Fig. 20 shows measured results of output power from coupler versus control voltage. One can observe that 40 dB linear dynamic range in both channels enables the receiver to deal with minimum signal level from -68 dBm in radar mode to -38 dBm in radio mode at the output of down-convertor. While the control voltage is set to be 0.78 V, by 30 dB gain of IF amplifiers the signal is fed into quadrature demodulator (HMC597LP4) at fixed signal level of 12 dBm.
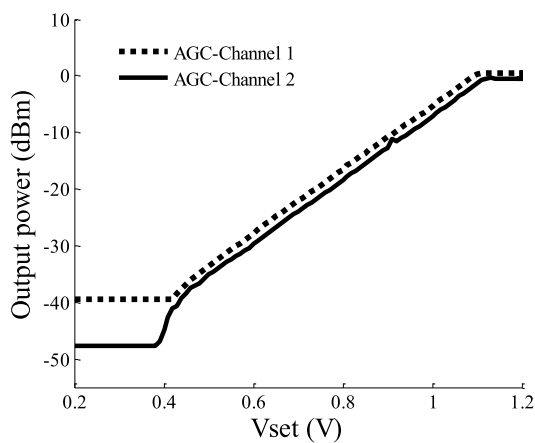

FIGURE 20. Gain control by two branches of AGC loop. Input power is -37.8 dBm in this measurement. The output of AGC loop is around -18 dBm for around 40 dB dynamic range of input power, provided that the Vset is fixed at 0.78 V.

D. Tx AND Rx ANTENNA

High gain Tx-antenna is adopted for this system on purpose. First, it can compensate the excessive path loss in radar propagation channel and give a sufficient range of coverage and second, it prevents unwanted ground-reflected echo due to its narrow beam in either horizontal or vertical planes. This antenna is realized by a 4×4 array of inset-fed patch elements as it is shown in Fig. 21. Feeding network encompasses 3 dB-splitters and distributes the transmitting signal with equal amplitude.

The layout is printed on Rogers-4350B substrate with 0.762 mm thickness. Antenna is optimized by 3D electromagnetic simulation software of computer simulation technology (CST) [41]. Fig. 22 shows that return loss is more than 10 dB for the whole specified band.

Measured and simulated radiation patterns in both E and H planed are shown in Fig. 23. Half power beam width (HPBW) of 20° along with 10 dB side lobe level in both planes isolates Tx antenna from the Rx antenna. The radar signal analysis in section III.C demonstrates that a minimum SNR of around 13 dB is required in order to guarantee the error variation
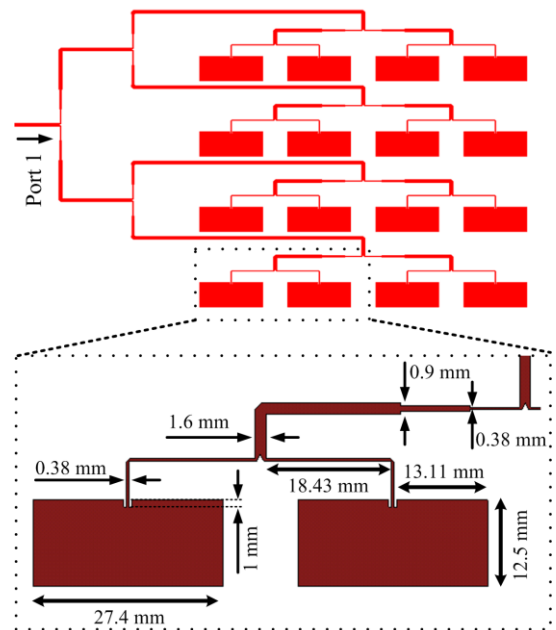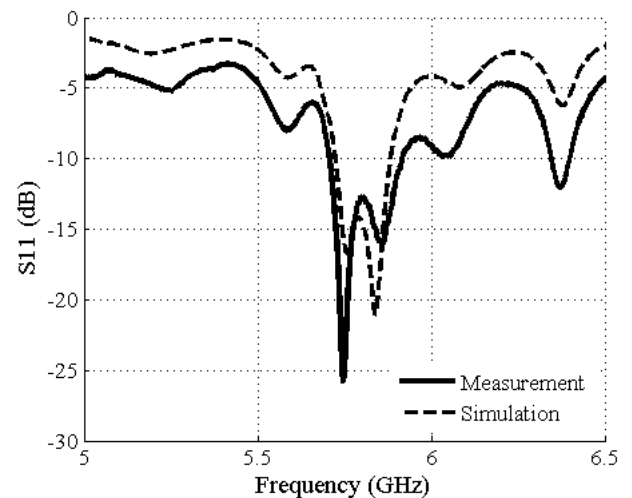

FIGURE 21. Building blocks of Tx antenna.

FIGURE 22. S11 of transmitter antenna.

of less than 1°. Therefore, the 10 dB side lobe level may not be enough and must be improved as it causes erroneous angle estimation. Nevertheless, this antenna is acceptable for system level measurement for this prototype.

Rx antenna is purposefully separated from Tx antenna to enhance the isolation and has a low gain in order to have sufficient angular range of coverage. This antenna is built up of two 15mm × 12.5mm patch elements that are fed by two separate SMA connectors from its backside. The layout is printed on Rogers-5870 with thickness of 3.175 mm. Both channels of antenna are matched to 50 Ohm and isolated from each other with measured return loss and isolation of more than 20 dB. According to the radiation patterns of one of the channels in both E- and H- planes the antenna demonstrates HPBW of 90° that satisfies the specified angular range of coverage, i.e. ±45°. In addition, back-lobe level is less
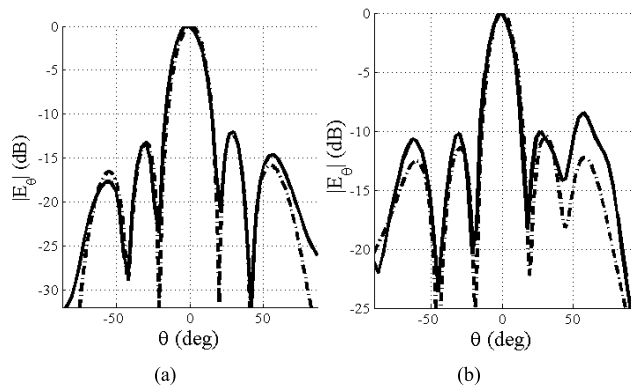
FIGURE 23. Normalized radiation pattern of Tx antenna in two planes; Solid line: measurements, dashed line: simulation. (a) E-plane. (b) H-plane.

than −15 dB that immunes the system from undesired echo from backside.

VII. SYSTEM-LEVEL MEASUREMENTS
A. RADIO COMMUNICATION
Fig. 24 shows the measurement setup for evaluating the performance of our transceiver when operating in radio mode. The IF modulated signal is generated using a vector signal generator (VSG) and is up-converted and transmitted using our prototyped Tx block and antenna.
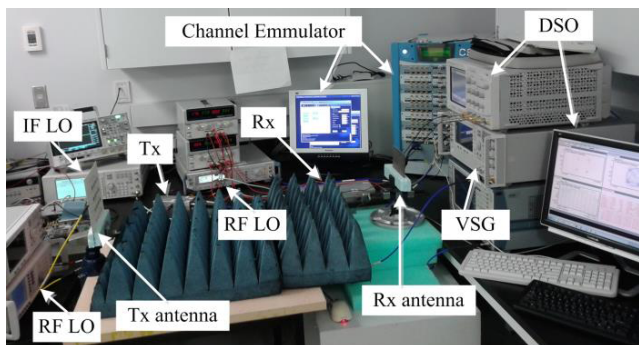

FIGURE 24. System measurement setup in communication mode; Channel emulator is used for SNR adjustment and the received SNR and EVM is measured using VSA in DSO.

The transmitted signal goes through a channel emulator (EB Propsim C8) by which the SNR of the received signal can be tuned before going through the Rx block. The demodulated signal at the output of the Rx is connected to a VSA that can plot the constellation diagram and also measure the SNR and EVM. The constellation diagram of the demodulated I and Q signals of four different modulation formats are demonstrated in Fig. 25. In addition, the EVM of received QPSK signal is measured versus different values of SNR and the result is plotted in Fig. 26. The theoretical EVM for QPSK signal can be expressed as a function of SNR by

$$EVM_{4QAM} = [\frac{1}{SNR} - 4\sqrt{\frac{1}{2\pi \times SNR}} e^{\frac{-SNR}{2}} + 2erfc(\sqrt{\frac{SNR}{2}})]^{1/2} \quad (10)$$
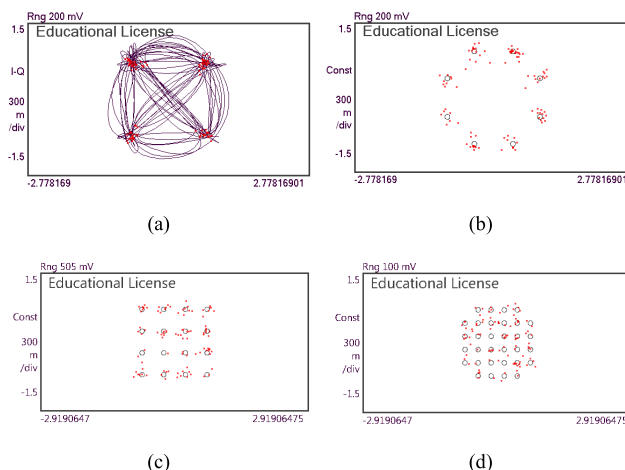

FIGURE 25. Measured constellation and EVM for different modulation schemes, when system is configured to operate in radio mode. (a) QPSK, EVM = 9.75%. (b) 8PSK, EVM = 14.56%. (c) 16 QAM, EVM = 10.9%. (d) 32 QAM, EVM = 8.83%.
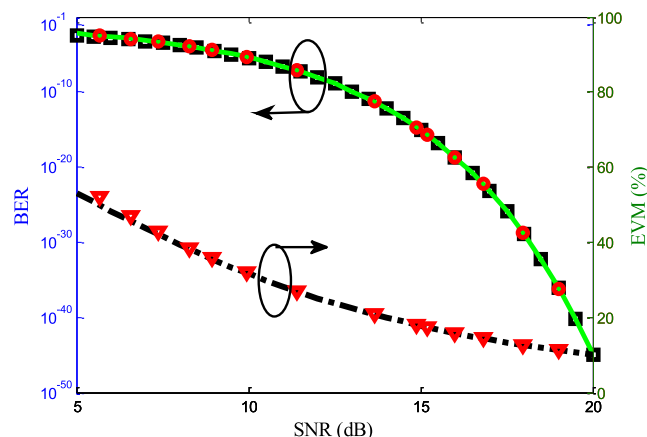

FIGURE 26. EVM and BER measurement results; -: BER (theory), square: BER converted from EVM (theory), o: BER converted from EVM (measurement), -.-: EVM (theory), triangle: EVM (measurement).

from [42, eq. (4)]. Both measured and theoretical EVM, plotted in Fig. 26 proved to be in excellent agreement.

EVM is actually the normalized error magnitude between measured constellation and the standard constellation [43, eq. (9)] and in the Gaussian noise model has inverse relation with the root square of SNR, i.e., $EVM = 1/\sqrt{SNR}$. This helps building a relation between measured EVM to BER.

Fig. 26 shows the BER values converted from measured EVM agree very well with the well-known theoretical BER for QPSK signal as a function of SNR that proves our system excellent capability in communication.

In another measurement for radio mode, the performance of the whole proposed transceiver is tested within a line of sight (LOS) communication setup shown in Fig. 27(a).

The Tx and Rx blocks of a single prototyped unit are playing the role of Tx and Rx blocks of two different on-board units which are supposed to communicate with
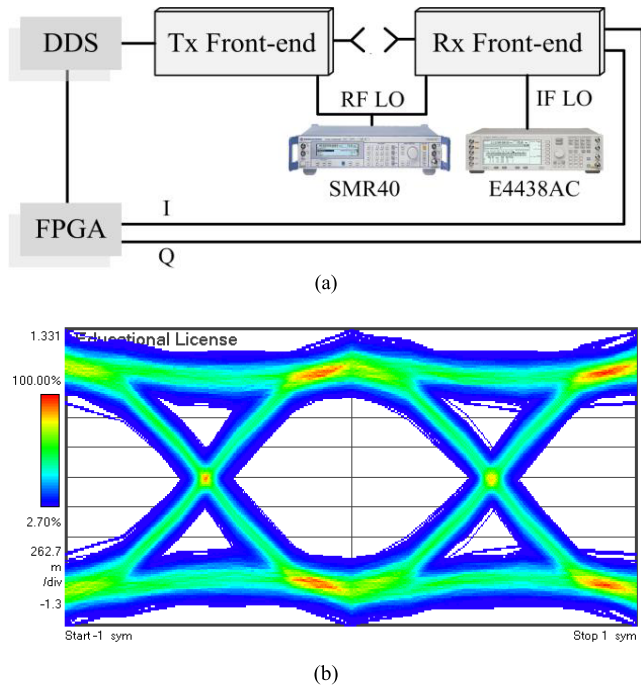
(a)

(b)

FIGURE 27. System measurement in radio mode; Measurement setup is arranged so that it emulates the received power of −59 dBm, associated to maximum communication range. (a) Measurement setup. (b) Measured eye-diagram in VSA89600.

(a)

(b)

FIGURE 28. Measurement results in communication mode; The received signals are match-filtered by an FIR filter with 4 taps and energy of unity. (a) Received signal and transmitted data. (b) After recovery.

each other. As in the previous measurement, the Tx block in this setup may also not share its IF carrier with the RX block as it is modulated in the back-end. Therefore, a separate signal generator is used as IF carrier for demodulating mixer in Rx block. In addition, RF LO is not prototyped in our system. So, another signal generator is used as a carrier for down-converting mixer.

Since the carrier recovery is not implemented devices are synchronized by sharing a single reference clock signal. Output of the transmitter is attenuated before radiation in order to emulate the received power of −59 dBm that associates to maximum communication range. The test signal is a BPSK modulated carrier with a data rate of 25 Mbps. Discriminated I and Q signals are probed by DSO and the measured eye-diagram is illustrated in Fig. 27(b). A wide eye opening along with a low distortion of symbols at zero crossing points demonstrates wide noise margin and safe sampling area.

In addition, the signals are sampled by ADCs at sampling rate of 100 MHz in order to have four samples per symbol. Since phase recovery algorithm is not implemented the carrier phase alignment is done by a phase shifter. The sampled signals as well as transmitted data are probed in FPGA via Signal-Tap2 software in Altera Quartus II package [44]. Given the proper operation of the whole system, the received signal must be a delayed version of the transmitted one. This can be readily observed in Fig. 28(a). Then, the received signal is match-filtered with a finite impulse response (FIR) filter of 4 taps and energy of unity. We can see
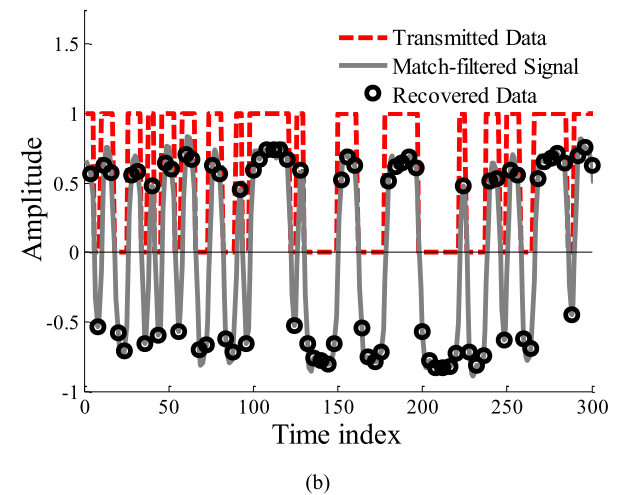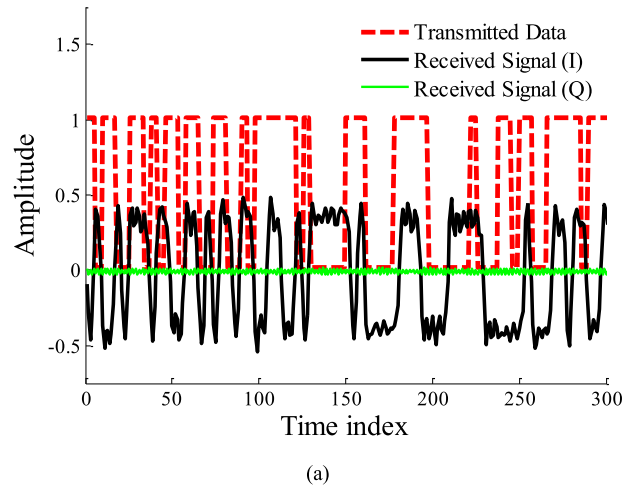
a very good agreement between the transmitted and recovered symbols in Fig. 28(b). In order to measure the SNR of the received symbols, the signal is processed further as follows: First, noise power in I and Q channels are calculated as P_{nI} and P_{nQ} by,

$$P_{nI} = \sigma^2(|I(k)|) = \frac{1}{N} \sum_{k=1}^{N} (|I(k)| - m(|I(k)|))^2$$

$$P_{nQ} = \sigma^2(|Q(k)|) = \frac{1}{N} \sum_{k=1}^{N} (|Q(k)| - m(|Q(k)|))^2 \quad (11)$$

where $\sigma^2(x)$ and $m(x)$ are variance and mean values of x, respectively. N is the total number of symbols which is 8184 in this measurement. The signal power per symbol is calculated by

$$P_s = \frac{1}{N} \sum_{k=1}^{N} I^2(k) - P_{nI}. \quad (12)$$

Measured $SNR = P_s/)P_{nI}+P_{nQ})$ is 14.36 dBm, which satisfies the predefined system specifications on BER very well.

B. RADAR SENSING

Several measurement setups are compromised on purpose as each of them addresses a specific parameter for which a contribution is made throughout this research.
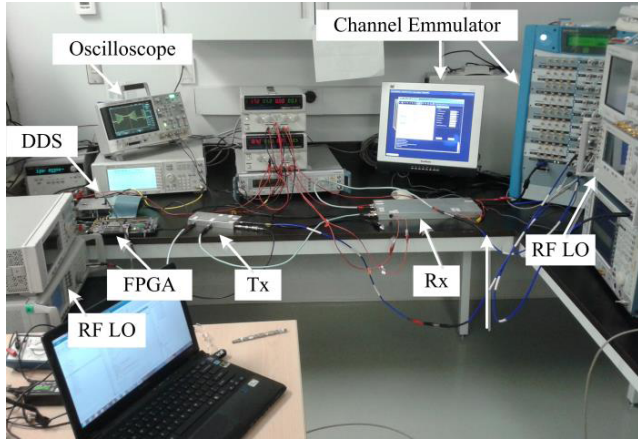

FIGURE 29. Radar mode measurements with channel emulator.

Fig. 29 shows the measurement setup of radar function which is built up to evaluate our simulated analysis of threshold detection. The channel emulator can emulate a pure-Doppler radar channel that resembles round trip propagation time and Doppler frequency shift with added interference noise at any desired SNR. Furthermore, mobile targets may be defined to move at constant velocity and positioned at a distance (R) that associates with propagation time (τ) by $R = c_0\tau/2$.

The SNR from PSD can be calculated as follows. Defining $S_1 = \sum_{j=0}^{N-1} w_j$ and $S_2 = \sum_{j=0}^{N-1} w_j^2$, the RMS value of PSD from N-point FFT of a signal with windowing (w_j) is known to be [30]

$$PSD_{rms}(f) = \frac{PS(f)}{ENBW} = \frac{\frac{|FFT(S_bw)|^2}{|S_1|^2}}{N\frac{S_2}{|S_1|^2} \times \frac{f_s}{N}}\left(\frac{V^2}{Hz}\right) \quad (13)$$

where PS is the power spectrum and the $ENBW$ is the effective noise bandwidth. Thus, SNR can be calculated by comparing the signal and noise power obtained from PSD

$$SNR(f_b) = \frac{PSD(f_b) \times ENBW}{E[PSD(N_o)] \times f_s} \quad (14)$$

where $E[.]$ and N_o denote the expectation function and the background noise, respectively.

Within the first measurement, the noise density is tuned for a single value of propagation time delay and Doppler in the emulator. One can observe the different noise levels in Fig. 30 that shows the PSD of beat signals for two cases with SNR of around 15 dB and 30 dB.
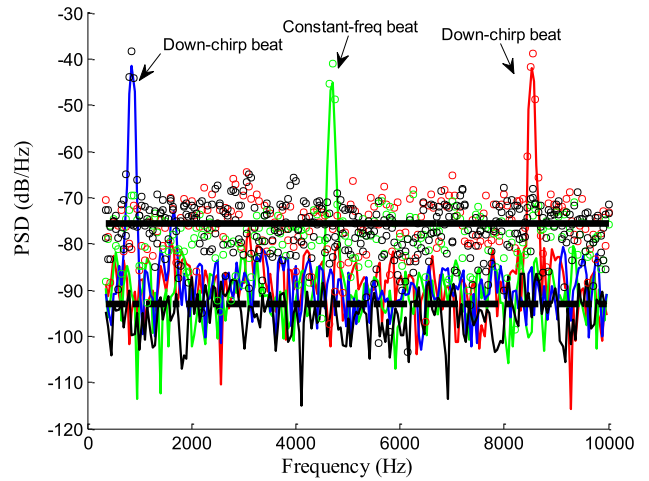
FIGURE 30. PSD (with Hanning window) of the measured beat signals with two different SNR; - : SNR=29.94 dB (case 1) o : SNR=15.04 dB (case 2), -.- : average noise level for case 1, − : average noise level for case 2.

TABLE 5. STD of range measurements.

SNR (dB)	Threshold (dB)					
	1.5	4.5	6.5	8.5	11.5	16.5
10.3	94.8	-	1.48	-	1.48	
14.5	101.6	32.89	1.37	-	1.37	
21.7	-	-	91.11	39.17	1.42	1.42
24.7			102.81	59.12	1.47	1.47

TABLE 6. STD of velocity measurements.

SNR (dB)	Threshold (dB)					
	1.5	4.5	6.5	8.5	11.5	16.5
10.3	34.85	-	1.26	-	1.26	
14.5	42.6	1.22	1.21	-	1.22	
21.6	-	-	17.6	1.24	1.24	1.24
24.7			9.03	1.26	1.26	1.26

More measurements were done with several distinct values of SNR keeping the value of time delay and velocity unchanged. Indeed, around 50 sets of beat signals for each value of SNR were saved for further processing. Then the STD of range and velocity was estimated with several values of threshold for each set of signals. It can be concluded from the results, tabulated in Table 3-4 that a minimum threshold of around 12 dB is essential to ensure correct detection which is in good agreement with our simulation results. Convergence of STD to half of range and velocity resolution validates our RadCom system ability in radar mode. It should be noted that the system in this measurement setup is first calibrated by measuring the internal delay when the Rx and Tx blocks are connected directly.

Another measurement in radar mode is carried out within the same testbed in order to assess our system's consistency in radar mode. Therefore, a few radar channels with different propagation time delay and Doppler shifts are set using the channel emulator. For this measurement, the data is collected from sampled signal provided by onboard ADCs by probing

from FPGA. Subsequently, captured signals are processed by FFT with zero padding in order to obtain desired information. FFT with length of 512 K is selected with the purpose of relaxing the error in estimation due to frequency resolution even though lower order of FFT may be used if the computation burden imposed by this high order FFT is not feasible in some practical applications.

TABLE 7. Measurement results of radar function.

Defined values		Measured values			
Delay (ns)	Velocity (m/s)	Delay (ns)			Velocity (m/s)
-----	-----	Before calibration	Error	After calibration	Without calibration
1500	30	1526	25.6	1499.2	30
1500	40	1526	25.8	1496.4	40.06
1500	50	1526	26	1499.6	50.12
2000	30	2026.4	26.4	2000	30
2000	40	2026.4	26.4	2000	40.06
2000	50	2026.4	26.4	2000	50.12
2750	30	2777.2	27.2	2750.8	30
2750	40	2777.2	27.2	2750.8	40.06
2750	50	2777.2	27.2	2750.8	50.12
3500	30	3527.6	27.6	3501.6	30
3500	40	3527.6	27.6	3501.6	40.06
3500	50	3528	28	3501.6	50.12

TABLE 8. Angle measurements.

Target's angle (deg)	Frequency bin (Hz)	Targets detected range (m)	Phase difference (rad)	Measured angle (deg) before & after calibration	
15°	95.03	1.900	1.0376	19.28°	14.11
30°	102.07	2.041	1.8151	35.21°	30.04
45°	159.9	3.198	2.4428	51.03°	45.86

The measurement results are presented in Table 7. As it was already observed in simulations and also the previous measurement, there is an almost constant error in estimated time delay due to the inherent delay between received and reference signals. The measured results after calibration agree very well with the defined values. This can fairly prove the consistency in radar functionalities.

With the purpose of evaluating the achievable range resolution, several targets are arranged in an indoor test-bed as it is shown in Fig. 31. Targets 3 and 4 as well as targets 5 and 6 are placed in a distance around the range resolution. The received beat signal is sampled by ADCs and read out of FPGA.

The range profile is estimated through FFT with zero padding as it is shown in Fig. 32. One can readily see that all targets are discriminated from each other. The range values shown in top x-axis in Fig. 32 is actually mapped from the frequency axis by solving the system functional equations in (2). Furthermore, since the targets are stationary no Doppler contribution is made to the beat frequencies, i.e. $f_{bu} = 2\Gamma R/c$. Hence, the range profile can be directly obtained from the
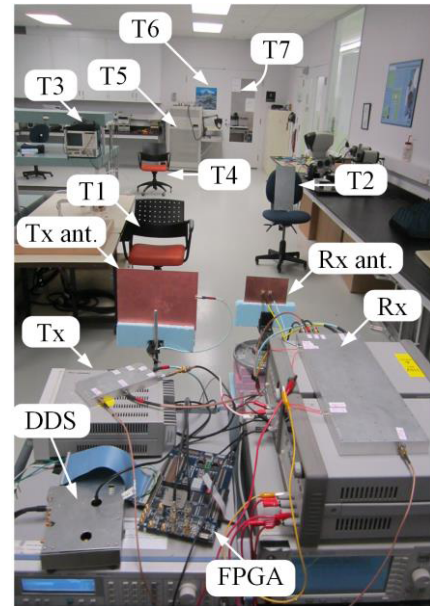

FIGURE 31. Measurement setup in lab. Targets 3 and 4 as well as targets 5 and 6 are deliberately positioned so close to each other to evaluate resolution in range estimation.
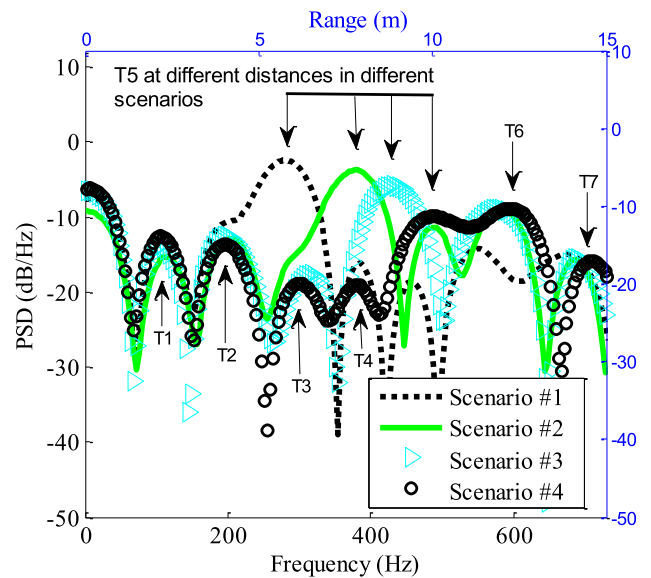

FIGURE 32. Range resolution and range profile measurement results; Scenario #1 (dot line) with T5 located at 5.5 m, Scenario #2 (solid line) with T5 located at 7.5 m, Scenario #3 (triangles) with T5 located at 8.5 m, Scenario #4 (circles) with T5 located at 9.5 m., Labels Ti (i=1:7) indicate the detected targets in Scenario #4 which is shown in Fig. 27. Measured range resolution between T3 and T4 is 1.526 m.

frequency axis of the spectrum of the received beat signal in the up-chirp time slot. The measured range resolution for the minimum distinguishable range of target is 1.52 m.

Additionally, in the same test-bed only T5 is placed in 4 different known distances in scenarios 1-4 and the range profile is obtained and added to Fig. 32. One can see as the target is placed further the corresponding peak appears in larger frequency.

TABLE 9. Comparison of different RadCom schemes.

| Reference	Integration domain	Bandwidth (MHz)	Radio signal	Radar signal	Range estimation	Velocity estimation	Angle estimation	Range resolution (measured)	Maximum data rate
[48] 5.9 GHz	Frequency	90	OFDM	OFDM	Yes	Yes	No	1.7 m (Theory)	27 Mbps
[14] 10 GHz	Frequency	500	PM-LFM	FMCW	Yes	Yes	No	63 cm	1 Mbps
[47] 7.5 GHz	Frequency	1000	OFDM	OFDM	Yes	Yes	No	34 cm	57 Mbps
[18] 60 Ghz	Frequency	3000	PPM	PPM	Yes	Yes	Yes	12.4 cm	200 Mbps
[50] 1.75 GHz	Time	60	ASK	FMCW	Yes	Yes	No	2.5 m (Theory)	1 Mbps
[16] 24 Ghz	Time	100	PM	TFMCW	Yes	Yes	No	1.65 m	50 MSPS
[15] 5.8 Ghz	Time	20	PM	TFMCW	Yes	Yes	No	7.5 m (Theory)	10 MSPS
This work 5.8 Ghz	Time	150	PM	TFMCW	Yes	Yes	Yes	1.53 m	75 MSPS
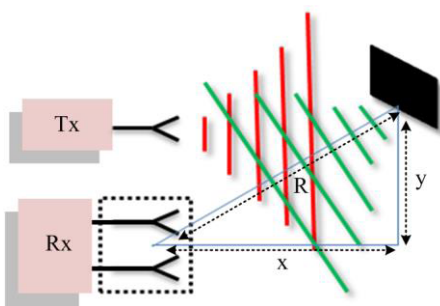
FIGURE 33. Angle measurement setup.

In order to evaluate the system capability in estimating the angular position of detected stationary objects, a special setup (sketched in Fig. 33) is arranged in our lab. True angular position with respect to the Rx antenna phase center can be roughly expected to be $tan^{-1}(y/x)$. The target is a small piece of metal and is located in an appropriate distance respecting Fresnel near field zone.

Phase and amplitude of the received beat signals after FFT for two different cases are plotted in Fig. 34 for reference. It should also be mentioned that the test is not carried out in anechoic chamber and the existence of adjacent in-lab objects increased the clutter level. One can see that as angle increases the distance of the target from Rx antenna increases and this makes the peak in amplitude to occur in larger values of frequency. Angles and distances are estimated through (3) and the results are listed in Table 8. The estimated range and angle can give us the position of the detected target as it is shown in Fig. 35. As we can see, there is around 5° of error between our estimated results and the true value. This can be attributed to a few reasons. First, the low SNR (measured roughly around 10 dB) or the possible small amount of inherent phase delay caused by PCB layout or cables can offset the phase difference.
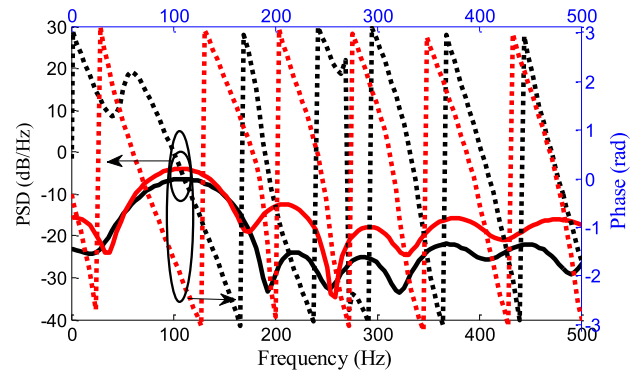
(b)   Angle=30
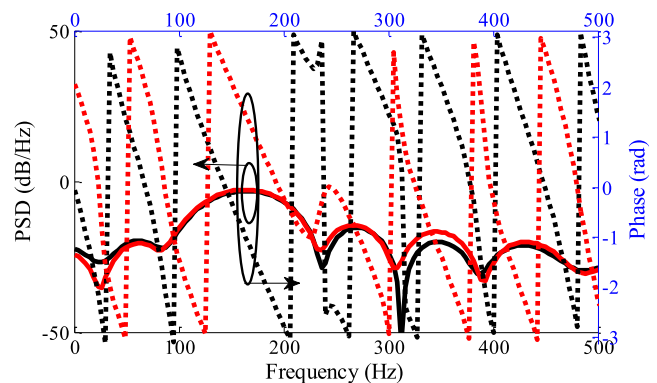
(c)   Angle=45

FIGURE 34. Angle measurement results; PSD (solid) and angle (dashed) of beat signals after FFT for two different positions of target. Red: channel 1, black: channel 2. The phase difference at peak frequencies should be used in (3) for calculating the angular position of the object. (a) Angle=30. (b) Angle=45.

Second, the exact expected value of angle in this test can only be determined with rough approximations because the reflected signal from a metal surface is a multipath
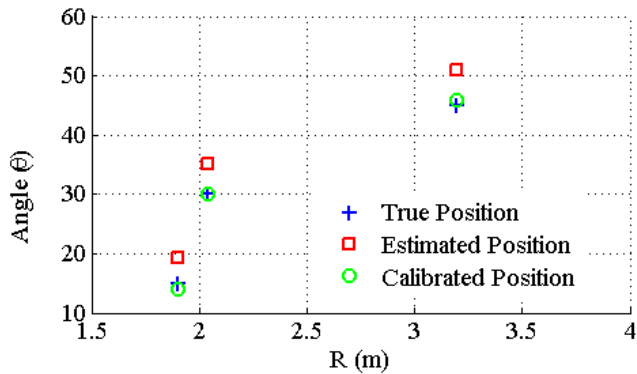
FIGURE 35. Measurement result in position estimation.

signal [49]. In fact, depending on the position of the node along the surface with strongest angular reflection, the angle estimation value by our prototyped system may change. This pinpoints a limitation of the system in exact angle detection when targets with large metal surface are present in the scenario. However, subtracting the average error from measured values yields rather accurate calibrated results.

VIII. CONCLUSION AND DISCUSSIONS

We have proposed and demonstrated a multifunctional system architecture taking all incompatibilities between radar and radio systems into account. It is capable of integrating the radar and communication functions required for future mobile data-fusion platform. In comparison to previous architectures, our system is improved to be capable of angle detection besides velocity and range estimation with enhanced resolution and accuracy. Our proposed multifunctional transceiver is prototyped and true multiple functionalities of the system are validated through several system-level simulations and measurements with the support of numerous results. Using an FPGA in back-end has made out system rather compact and capable of a flexible functional reconfiguration upon data fusion.

In Table 9, this work is compared with the state of the art reported works for different integration schemes of time and frequency in terms of the variety of functions that was integrated with their proposed scheme. We can see that our work outweighs because it detects angle and also the measured range resolution is around 1.5 m, utilizing only 150 MHz. It should be noted that our system performance in communication with data rate of up to only 25 MSPS is verified due to limited maximum clock frequency of our onboard ADC's (i.e. 100 MHz). Among the references, localization technique proposed by [18] which is capable of complete positioning demands for larger bandwidth resources and is mostly appropriate for short range applications.

Nevertheless, the proposed transceiver scheme is still subject to further developments. For example, the proposed interferometry approach for angle detection might have some limitations in a real scenario with multiple targets especially when two close targets are moving with identical speeds and the beat frequencies may not be discriminated.

Despite these limitations, angle detection based on Doppler phase difference was considered as the best candidate at this stage of research for multi-functional transceivers, due to its simplicity. Evolving phased-array or digital beam forming (DBF) technique has demonstrated reliable performance when applied to automotive radars, [23], [45], [46]. However, a considerable improvement on further unification of the RF front-end of RadCom transceivers, the Rx in particular, should first be made if the undesired complexity of beam forming systems is to be avoided. In addition, a significant research effort can be anticipated on the antenna part by developing a reconfigurable antenna with variable gain. Furthermore, the RadCom system needs a high gain antenna when functioning as radar while a low gain with wide beamwidth is desirable in the radio mode.

Therefore, the proposed architecture can ignite the further developments of future sensor-fused automotive and vehicular radars with the full ability of high-speed communication [2] as well as DSRC devices with an expanded ability of collision avoidance and other functionalities.

ACKNOWLEDGMENT

REFERENCES

[1] R. Bishop, *Intelligent Vehicle Technology and Trends*, 1st ed. Norwood, MA, USA: Artech House, 2005, pp. 1–6.
[2] R. H. Rasshofer and K. Naab, "77 GHz long range radar systems status, ongoing developments and future challenges," in *Proc. EURAD*, 2005, pp. 161–164.
[3] B. Fleming, "Recent advancement in automotive radar systems [automotive electronics]," *IEEE Veh. Technol. Mag.*, vol. 7, no. 1, pp. 4–9, Mar. 2012.
[4] R. Cager, Jr., D. T. LaFlame, and L. C. Parode, "Orbiter *Ku*-band integrated radar and communications subsystem," *IEEE Trans. Commun.*, vol. 26, no. 11, pp. 1604–1619, Nov. 1978.
[5] S. Lindenmeier, K. Boehm, and J. F. Luy, "A wireless data link for mobile applications," *IEEE Microw. Wireless Compon. Lett.*, vol. 13, no. 8, pp. 326–328, Aug. 2003.
[6] X. Yin *et al.*, "Embedded ranging system in ISM band," *Electron. Lett.*, vol. 44, no. 17, pp. 1043–1045, Aug. 2008.
[7] S. J. Xu, Y. Chen, and P. Zhang, "Integrated radar and communication based on DS-UWB," in *Proc. 3rd Int. Conf. Ultrawideband Ultrashort Impulse Signals*, Sevastopol, Ukraine, Sep. 2006, pp. 142–144.
[8] Z. Lin and P. Wei, "Pulse amplitude modulation direct sequence ultra wideband sharing signal for communication and radar systems," in *Proc. 7th Int. Symp. Antennas, Propag. EM Theory*, Guilin, China, Oct. 2006, pp. 1–5.
[9] M. Jamil, H. J. Zepernick, and M. I. Pettersson, "On integrated radar and communication systems using oppermann sequences," in *Proc. IEEE Military Commun. Conf.*, San Diego, CA, USA, Nov. 2008, pp. 1–6.
[10] K. Mizui, M. Uchida, and M. Nakagawa, "Vehicle-to-vehicle communication and ranging system using spread spectrum technique (Proposal of Boomerang Transmission System)," in *Proc. 43rd IEEE Veh. Technol. Conf.*, Secaucus, NJ, USA, May 1993, pp. 335–338.
[11] Z. Lin and P. Wei, "Pulse position modulation time hopping ultra wideband sharing signal for radar and communication system," in *Proc. Int. Conf. Radar*, Shanghai, China, Oct. 2006, pp. 1–4.

[12] E. Cianca and B. Gupta, "FM-UWB for communications and radar in medical applications," *Wireless Pers. Commun.*, vol. 51, no. 4, pp. 793–809, Dec. 2009.

[13] G. N. Saddik, R. S. Singh, and E. R. Brown, "Ultra-wideband multifunctional communications/radar system," *IEEE Trans. Microw. Theory Techn.*, vol. 55, no. 7, pp. 1431–1437, Jul. 2007.

[14] K. Konno and S. Koshikawa, "Millimeter-wave dual mode radar for headway control in IVHS," in *Proc. IEEE MTT-S Int. Microw. Symp.*, Denver, CO, USA, Jun. 1997, pp. 1261–1264.

[15] L. Han and K. Wu, "Multifunctional transceiver for future intelligent transportation systems," *IEEE Trans. Microw. Theory Techn.*, vol. 59, no. 7, pp. 1879–1892, Jul. 2011.

[16] L. Han and K. Wu, "24-GHz integrated radio and radar system capable of time-agile wireless communication and sensing," *IEEE Trans. Microw. Theory Techn.*, vol. 60, no. 3, pp. 619–631, Mar. 2012.

[17] L. Cheng, B. E. Henty, D. D. Stancil, F. Bai, and P. Mudalige, "Mobile vehicle-to-vehicle narrow-band channel measurement and characterization of the 5.9 GHz dedicated short range communication (DSRC) frequency band," *IEEE J. Sel. Areas Commun.*, vol. 25, no. 8, pp. 1501–1516, Oct. 2007.

[18] M. Bocquet *et al.*, "A multifunctional 60-GHz system for automotive applications with communication and positioning abilities based on time reversal," in *Proc. Eur. Radar Conf. (EuRAD)*, Paris, France, Sep./Oct. 2010, pp. 61–64.

[19] Y. L. Sit, C. Sturm, J. Baier, and T. Zwick, "Direction of arrival estimation using the MUSIC algorithm for a MIMO OFDM radar," in *Proc. IEEE Radar Conf. (RADAR)*, May 2012, pp. 0226–0229.

[20] J. Moghaddasi and K. Wu, "Improved joint radar-radio (RadCom) transceiver for future intelligent transportation platforms and highly mobile high-speed communication systems," in *Proc. IEEE Int. Wireless Symp.*, Beijing, China, Apr. 2013, pp. 1–4.

[21] N. Levanon and E. Mozeson, *Radar Signals*. New York, NY, USA: Wiley, 2004.

[22] A. Lin and H. Ling, "Doppler and direction-of-arrival (DDOA) radar for multiple-mover sensing," *IEEE Trans. Aerosp. Electron. Syst.*, vol. 43, no. 4, pp. 1496–1509, Oct. 2007.

[23] J. Hatch, A. Topak, R. Schnabel, T. Zwick, R. Weigel, and C. Waldschmidt, "Millimeter-wave technology for automotive radar sensors in the 77 GHz frequency band," *IEEE Trans. Microw. Theory Techn.*, vol. 60, no. 3, pp. 845–860, Mar. 2012.

[24] V. Winkler, "Range Doppler detection for automotive FMCW radars," in *Proc. Eur. Microw. Conf.*, Oct. 2007, pp. 166–169.

[25] E. Hyun, W. Oh, and J.-H. Lee, "Multi-target detection algorithm for FMCW radar," in *Proc. IEEE Radar Conf.*, May 2012, pp. 0338–0341.

[26] S. Miyahara, "New algorithm for multiple object detection in FM-CW radar," SAE Tech. Paper 2004-01-0177, Mar. 2004.

[27] *MATLAB*, MathWorks, Natick, MA, USA, 2013.

[28] E. Hyun and J.-H. Lee, "A meothod for multi-target range and velocity detection in automotive FMCW radar," in *Proc. 12th Int. IEEE Conf. Intell. Transp. Syst.*, Oct. 2009, pp. 1–5.

[29] A. Bazzi, C. Kärnfelt, A. Péden, T. Chonavel, P. Galaup, and F. Bodereau, "Estimation techniques and simulation platforms for 77 GHz FMCW ACC radars," *Eur. Phys. J., Appl. Phys.*, vol. 57, no. 1, pp. 1–16, Jan. 2012.

[30] G. Heinzel, A. Rüdiger, and R. Schilling, "Spectrum and spectral density estimation by the discrete Fourier transform (DFT), including a comprehensive list of window functions and some new at-top windows," Max Planck Inst. Gravitational Phys., Potsdam, Germany, Tech. Rep., Feb. 2002. [Online]. Available: http://www.rssd.esa.int/SP/LISAPATHFINDER/docs/Data_Analysis/GH_FFT.pdf.

[31] *Amendment of Parts 2 and 90 of the Commission's Rules to Allocate the 5.850–5.925 GHz Band to the Mobile Service for Dedicated Short Range Communications of Intelligent Transportation Services*, document FCC 03-324, Federal Communications Commissions, Feb. 2004.

[32] H. Rohling, "Some radar topics: waveform design, range CFAR and target recognition," in *Advances in Sensing With Security Applications*. Hamburg, Germany: Technical Univ. Hamburg-Harburg, 2006, pp. 293–322.

[33] H. Rohling, "Radar CFAR thresholding in clutter and multiple target situations," *IEEE Trans. Aerosp. Electron. Syst.*, vol. AES-19, no. 4, pp. 608–621, Jul. 1983.

[34] J. G. Proakis, *Digital Communications*, 4th ed. New York, NY, USA: McGraw-Hill, 2001, sec. 5.5.2, pp. 315–318.

[35] R. Ebelt *et al.*, "On the performance of pulsed frequency modulated UWB local positioning systems," in *Proc. IEEE MTT-S Int. Microw. Symp.*, Baltimore, MD, USA, Jun. 2011, pp. 1–4.

[36] T. Long, Y. Wang, and T. Zeng, "Signal-to-noise ratio in stretch processing," *IET Electron. Lett.*, vol. 46, no. 10, pp. 720–722, 2010.

[37] *Advanced Design System (ADS)*, Agilent Technol., Santa Clara, CA, USA, 2009.

[38] Agilent Technology. (May 2005). *8 Hint for Making and Interpreting EVM Measurements*. [Online]. Available: http://www.home.agilent.com/agilent/home.jspx?cc=US&lc=eng.

[39] I. Rosu. (Mar. 2013). *Automatic Gain Control (AGC) in Receivers*. [Online]. Available: http://www.qsl.net.

[40] D. Whitlow. (Mar. 2013). *Design and Operation of Automatic Gain Control Loops for Receivers in Modern Communication Systems*. [Online]. Available: http://www.analog.com.

[41] *Computer Simulation Technology (CST)*, AG, Darmstadt, Germany, 2011.

[42] J. G. Proakis, *Digital Communications*, 4th ed. New York, NY, USA: McGraw-Hill, 2001, sec. 9.2, pp. 554–556.

[43] Z.-Y. Zhang, Y.-R. Wei, and K. Wu, "Broadband millimeter-wave single balanced mixer and its applications to substrate integrated wireless systems," *IEEE Trans. Microw. Theory Techn.*, vol. 60, no. 3, pp. 660–669, Mar. 2012.

[44] *Altera Quartus II, V11*, Altera, San Jose, CA, USA, 2011.

[45] M. Steinhauer, H.-O. Ruo, H. Irion, and W. Menzel, "Millimeter-wave-radar sensor based on a transceiver array for automotive applications," *IEEE Trans. Microw. Theory Techn.*, vol. 56, no. 2, pp. 261–269, Feb. 2008.

[46] B.-H. Ku *et al.*, "A 77–81-GHz 16-element phased-array receiver with ±50° beam scanning for advanced automotive radars," *IEEE Trans. Microw. Theory Techn.*, vol. 62, no. 11, pp. 2823–2832, Nov. 2014.

[47] D. Garmatyuk, J. Schuerger, and K. Kauffman, "Multifunctional software-defined radar sensor and data communication system," *IEEE Sensors J.*, vol. 11, no. 1, pp. 99–106, Jan. 2011.

[48] L. Reichardt, C. Sturm, F. Grunhaupt, and T. Zwick, "Demonstrating the use of the IEEE 802.11P car-to-car communication standard for automotive radar," in *Proc. 6th Eur. Conf. Antennas Propag. (EUCAP)*, Mar. 2012, pp. 1576–1580.

[49] R. Feger, C. Pfeffer, W. Scheiblhofer, C. M. Schmid, M. J. Lang, and A. Stelzer, "A 77-GHz cooperative radar system based on multi-channel FMCW stations for local positioning applications," *IEEE Trans. Microw. Theory Techn.*, vol. 61, no. 1, pp. 676–684, Jan. 2013.

[50] L. Xie, X. Yin, L. Yang, C. Lu, and H. Zhao, "Multifunctional communication transceiver with distance measurement capability," in *Proc. IEEE Asia-Pacific Microw. Conf.*, Sendai, Japan, Nov. 2014, pp. 405–407.

JABER MOGHADDASI received the B.Sc. (Hons.) degree in electrical engineering from the K. N. Toosi University of Technology, Tehran, Iran, in 2010.

He is currently pursuing the Ph.D. degree in electrical engineering with the University of Montreal. His current research interests include multifunctional systems and reconfigurable RF front-end architectures.

He joined the Poly-Grames Research Center, École Polytechnique de Montréal, University of Montreal, as a Research Assistant in 2011. He has authored several peer-reviewed papers and holds three patents. He was a recipient of some national and/or international awards, including the best paper award in the IEEE Microwave Theory and Techniques Society (MTT-S) International Wireless Symposium (2013) in Beijing, China, the MTT-S Ph.D. Initiative Award in the IEEE International Microwave Symposium (2012), the Student Challenge Prize in European Microwave Week (2013) in Nuremberg, Germany, the first prizes in the student research poster competitions in both CREER-2011 and CREER-2013, and the second prize in the CREER-2015 Symposium in Montreal, Canada. He also received the Canadian NSERC-Perswade Fellowship in 2014.

He joined the Advanced-Concept Group, BlackBerry Company, Waterloo, ON, Canada, in 2015, developing wideband receiver ICs through CMOS technology.

He was a member of a team cooperating with Huawei Company in a research project for next generation V/E band radio architectures in 2014.

KE WU (M'87–SM'92–F'01) received the B.Sc. (Hons.) degree in radio engineering from the Nanjing Institute of Technology, China, in 1982, and the D.E.A. and Ph.D. (Hons.) degrees in optics, optoelectronics, and microwave engineering from the Institut National Polytechnique de Grenoble and the University of Grenoble, France, in 1984 and 1987, respectively. He was the Founding Director of the Center for Radiofrequency Electronics Research of Quebec (Regroupement Stratégique of FRQNT). He has been the Director of the Poly-Grames Research Center, École Polytechnique de Montréal, University of Montreal. He is currently a Professor of Electrical Engineering, the Tier-I Canada Research Chair in RF and Millimeter-Wave Engineering, and the NSERC-Huawei Industrial Research Chair in Future Wireless Technologies with the University of Montreal. He has also held guest, visiting, and honorary professorship at many universities around the world. He has authored or co-authored over 1000 referred papers, a number of books/book chapters, and holds more than 30 patents. His current research interests include substrate integrated circuits, antenna arrays, advanced CAD and modeling techniques, non-linear wireless technologies, wireless power transmission and harvesting, and development of RF and millimeter-wave transceivers and sensors for wireless systems and biomedical applications. He is also interested in the modeling and design of microwave and terahertz photonic circuits and systems.

Dr. Wu is a member of the Electromagnetics Academy, the Sigma Xi Honorary Society, and URSI. He is a fellow of the Canadian Academy of Engineering and the Royal Society of Canada (The Canadian Academy of the Sciences and Humanities). He has held key positions in and has served on various panels and international committees, including the Chair of the technical program committees, international steering committees, and international conferences/symposia. In particular, he was the General Chair of the 2012 IEEE MTT-S International Microwave Symposium. He has served on the Editorial/Review Boards of many technical journals, transactions, proceedings, and letters, and scientific encyclopedia, including editors and guest editors. He was the Chair of the joint IEEE Chapters of MTTS/APS/LEOS in Montreal. He is the Chair of the newly re-structured IEEE MTT-S Montreal Chapter. He was an Elected IEEE MTT-S AdCom Member from 2006 to 2015, and served as the Chair of the IEEE MTT-S Transnational Committee, the Member and Geographic Activities Committee, and the Technical Coordinating Committee, among many other AdCom functions. He is the 2016 IEEE MTT-S President. He is the inaugural three-year representative of North America as a member of the European Microwave Association General Assembly. He was a recipient of many awards and prizes, including the first IEEE MTT-S Outstanding Young Engineer Award, the 2004 Fessenden Medal of the IEEE Canada and the 2009 Thomas W. Eadie Medal of the Royal Society of Canada, the Queen Elizabeth II Diamond Jubilee Medal in 2013, the 2013 FCCP Education Foundation Award of Merit, the 2014 IEEE MTT-S Microwave Application Award, the 2014 Marie-Victorin Prize (Prix du Quebec—the highest distinction of Québec in the natural sciences and engineering), the 2015 Prix d'Excellence en Recherche et Innovation of Polytechnique Montréal, and the 2015 IEEE Montreal Section Gold Medal of Achievement. He was an IEEE MTT-S Distinguished Microwave Lecturer from 2009 to 2011.

● ● ●